https://doi.org/10.5194/egusphere-2025-998
Preprint. Discussion started: 26 March 2025
© Author(s) 2025. CC BY 4.0 License.

Modeling water column gas transformation, migration and atmospheric flux from seafloor seepage

Knut Ola Dølven[1], Håvard Espenes[2,3,*], Alfred Hanssen[1,*], Muhammed Fatih Sert[1], Magnus Drivdal[2], Achim Randelhoff[2], and Bénédicte Ferré[1]

[1]Department of Geosciences, UiT The Arctic University of Norway, Tromsø, Norway
[2]Ocenaography section, Akvaplan NIVA, Tromsø, Norway
[3]SINTEF Ocean, Trondheim, Norway
[*]These authors contributed equally to this work.

Correspondence: Knut Ola Dølven (knut.o.dolven@uit.no)

Abstract. Understanding the fate of gas seeping from the seafloor is crucial for assessing the environmental impact of natural and anthropogenic seep systems, such as CH_4 cold seeps or leaks from gas wells or future carbon capture projects. We present a comprehensive modelling framework that integrates physical, biological and chemical processes to estimate the 3-dimensional dissolved concentration and total atmospheric flux of gas from seafloor seeps. The framework consists of two main steps: 1) A gas phase model that estimates free gas dissolution and direct atmospheric flux at the seep site, and 2) a concentration model that combines particle dispersion modelling, an adaptive-bandwidth kernel density estimator, and customizable process modules. Using this framework, we successfully modeled the concentration field and atmospheric flux of CH_4 between May 20 and June 20, 2018, from a natural seep site located at 200 meters depth offshore Northwestern Norway. Results show that dissolved gas is primarily advected northeastward along the coast, spreading effectively across the shelves, reefs, and entering open fjord systems. Within a few days, the vertical CH_4 concentration profile is near inverted, with peak concentrations close to the sea surface – facilitating atmospheric exchange. Diffusive emissions are spread out over large areas ($>10^5 km^2$) and exceeds the local free gas flux by more than threefold ($\sim$0.76%) during the modeling period while $\sim$40% of the CH_4 remains in the water column. Although high uncertainties remains regarding microbial oxidation rates, microbes represent the main sink of CH_4, converting $\sim$60% of dissolved CH_4 to CO_2 during the modeling period. These findings highlight the importance of accounting for dissolved gas from seeps when evaluating their impact on atmospheric emissions and ecosystem interactions. Our framework provides a globally applicable tool that incorporates free and dissolved gas dynamics and flexible inclusion of chemical and biological processes, supporting improved understanding and ability to quantify environmental impacts of seabed gas seeps in the future.

1 Introduction

Estimates of the contribution of seafloor gas seepage to atmospheric emissions and its impact on ocean environments are highly uncertain due to limited data and understanding of gas transformation and transport mechanisms in the water column. Atmospheric measurements are currently the only approach for estimating total atmospheric emissions from seep areas (e.g.

https://doi.org/10.5194/egusphere-2025-998
Preprint. Discussion started: 26 March 2025
© Author(s) 2025. CC BY 4.0 License.

Myhre et al., 2016). These typically rely on either ship measurements or large-scale atmospheric inversion models, where the former only gives *in situ* flux, and the latter is unable to estimate dispersed sources and/or weaker point sources precisely due to its rough scale and inability to completely decouple atmospheric sources from sinks (Thompson and Stohl, 2014). Quantifying dissolved gas in the water column usually involves measuring dissolved gas via water samples (e.g. Silyakova et al., 2020) or using *in situ* sensors (e.g. Gentz et al., 2014) which can be time-consuming and often result in poor data coverage. New modeling tools for constraining the environmental impacts of current and future seabed gas seepage from both natural and man made sources are therefore needed.

Gas released at the seabed can enter the atmosphere directly as free gas (bubbles) or via diffusive equilibrium of dissolved gas that has reached the sea surface. To estimate the total atmospheric emissions from a seabed seep and its dissolved distribution in the water column, one must be able to model both pathways simultaneously. Gas contained in bubbles can dissolve rapidly in ambient water and be exchanged with alien gases across the bubble rim. Additionally, chemical and biological processes can modify local dissolved gas content. Estimating the gas distribution in the water column and total atmospheric flux therefore requires a flexible framework which can integrate processes governing the gas phase dynamics and the hydrodynamics, accommodate atmospheric exchange and other phenomena that modify water column gas content. Previous modeling efforts have focused on modeling either of the pathways and have been constrained in terms of dimensionality and/or integration of processes, such as regional hydrodynamics (e.g McGinnis et al., 2006; Graves et al., 2015; Silyakova et al., 2020). Our aim is to provide a framework which can integrate all key processes governing free and dissolved transport and transformation of seeped gas to provide a full 3-d concentration field in the water column and total atmospheric release estimates.

Our approach uses *in situ* seabed seepage data and integrates a gas phase model with a hydrodynamic model using particle dispersion modeling. This enables simultaneous estimation the total free and diffusive atmospheric gas release caused by the observed seeps and the three-dimensional (3D) distribution of gas in the water column. The approach also offers flexible inclusion of atmospheric flux and chemical and biological process modules affecting dissolved gas content in the water column. Explicit concentrations (molecules per volume) are obtained using kernel density estimation and atmospheric flux estimations obtained using a bulk model. We tested the framework by quantifying direct and diffusive atmospheric fluxes as well as 3D dissolved gas distribution between May 20 and June 20, 2018 for a methane (CH_4) seep area offshore Northwestern Norway.

2 Method

Our goals are two-fold: i) Calculate the combined total amount of seep-derived gas that reaches the atmosphere - both direct free gas release and ventilation of dissolved gas, and ii) Estimate the impact of seeped gas on the scalar dissolved gas concentration field, i.e. we seek the anomaly $\Phi'(x,y,z,t)$=$\Phi(x,y,z,t) - \Phi_o(x,y,z,t)$, where $\Phi(x,y,z,t)$ denotes the total concentration and $\Phi_o(x,y,z,t)$ is the background concentration.

The outlined goals are achieved by adapting and integrating existing and new models, of which output from one model serves as result or feeds another model. We first use seabed gas volume flux data and a two-phase gas model to calculate the gas dissolution rates and direct atmospheric gas (bubble) release. Dissolved injection rate output from the gas phase model

https://doi.org/10.5194/egusphere-2025-998
Preprint. Discussion started: 26 March 2025
© Author(s) 2025. CC BY 4.0 License.

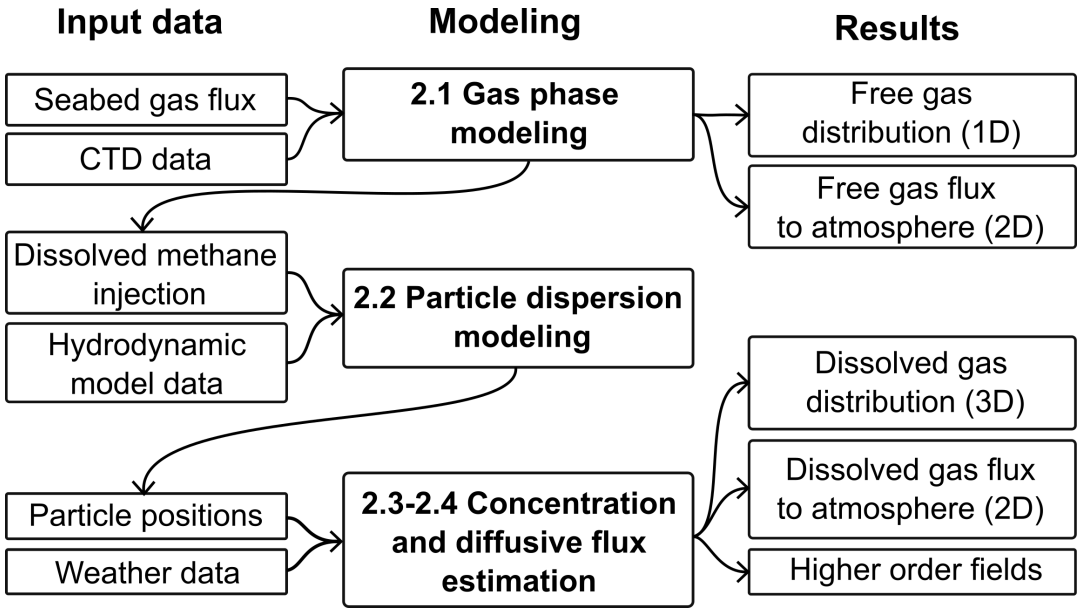

Figure 1. Model framework flowchart. The emboldened modeling steps and associated numbers refer to the four subsections of the Methods section. The "D" in the results column refers to spatial dimensions.

then feeds a concentration model that combines an existing dispersion modeling framework with an adaptive kernel density estimator, including an atmospheric flux module and options for water column process modules. Figure 1 shows the complete framework, with input data in the left column, the modeling steps in the center column, and the final results in the right column. Each modeling section is detailed in the corresponding subsection.

2.1 Gas phase modeling

Free atmospheric gas fluxes and dissolved gas profiles injected to the water column are initially modeled for each observed seep using the seabed free gas flux data and the M2PG1 gas phase model (Jansson et al., 2019). M2PG1 provides an integrated solution of dissolved and free gas in a 1-dimensional water column, with sources and sinks at both horizontal and vertical model boundaries. It simultaneously models gas exchange, dissolution, and associated dissolved gas concentration of five gas species (methane CH_4, Argon Ar, Carbon dioxide CO_2, Nitrogen N_2, and Oxygen O_2) across a user-defined initial spectrum of bubble sizes. The bubble size spectrum and gas distribution across this spectrum freely vary across the spatio-temporal model domain. The model includes several bubble shape and rising speed models, microbial oxidation of CH_4 using first order kinetics (Griffiths et al., 1982; Chan et al., 2019), diffusive exchange with the atmosphere, dissolved transport due to vertical turbulent exchange of water masses, as well as loss due to advection across the model boundary (Jansson et al., 2019). While dynamic solutions are permissible in M2PG1, we have opted for a steady state solution in our modeling framework.

https://doi.org/10.5194/egusphere-2025-998
Preprint. Discussion started: 26 March 2025
© Author(s) 2025. CC BY 4.0 License.

The input parameters include seabed gas flux, bubble characteristics (size distribution, rising speed, dirtiness, flatness), temperature, salinity, microbial CH_4 oxidation rate coefficients (MOx), ambient dissolved gas concentrations (for all five gases), vertical mixing (turbulent) and local ocean currents. Seabed free gas flux data can in theory be obtained by any means available, although hydroacoustics has been used extensively due to its simple use and large coverage (e.g. Ferré et al., 2020).

In our implementation of M2PG1 we used an estimation technique to determine the horizontal model domain size, which was previously ambiguous in the initial M2PG1 model (Jansson et al., 2019) and could cause significant exchange rate errors. Our method removes this ambiguity by estimating the horizontal bubble plume extent based on local conditions. Details are provided in Appendix A.

The steady-state output from the M2PG1 simulation provides two key results: i) direct atmospheric gas flux and ii) injection rates of dissolved gas to the surrounding water column. The former is a direct output in M2PG1 and the latter, which are key input for the concentration modeling steps (Sect 2.3-2-4), can be derived from the dissolved gas concentration profiles by calculating the dissolved gas loss q [mol s^{-1}] to the water column at the downstream boundary of each M2PG1 grid cell. The steady-state mass flux assumption gives:

$$q = A^{\perp}_{\mathcal{M}} U(\varphi_{\mathcal{M}} - \varphi_b), \tag{1}$$

where $A^{\perp}_{\mathcal{M}}$ [m^2] is the vertical grid cell area (Appendix A), U[m s^{-1}] the current speed, $\varphi_{\mathcal{M}}$ [mol m^{-3}] the estimated concentration within the grid cell and φ_b [mol m^{-3}] the assumed concentration at the upstream boundary.

2.2 Particle dispersion modeling

To estimate the dissolved gas field we must model the advection and spread of the dissolved gas from the release site. We chose to simulate the transport and dispersion of the gas from the release site using OpenDrift, which is a Lagrangian particle trajectory modeling software (Dagestad et al., 2018).

In practice, this means that we divide the released CH_4 over a discrete number of particles, and update the particle positions at discrete time steps t_n for time-steps $n = 1, 2, 3, ..., N$. Each timestep is separated by a time interval Δt. Furthermore, we let $S[n]$ be the number of virtual particles seeded at predefined locations (the relase sites) at each time step. This generates a total of $Z = \sum_{n=1}^{N} S[n]$ particles indexed by $\zeta = 1, 2, 3, ..., Z$. OpenDrift calculates the trajectory of each particle individually by solving the Lagrangian form of the advection-diffusion equation

$$\frac{\partial \boldsymbol{\eta}}{\partial t} = \mathbf{U}_{\mu}(\boldsymbol{\eta}, t) + \mathbf{U}_{s}(\boldsymbol{\eta}, t), \tag{2}$$

where $\boldsymbol{\eta}$ is the particle position and $\mathbf{U}_{\mu}$ and $\mathbf{U}_{s}$ are advective (mean) and diffusive (stochastic) velocity vectors, respectively. The advective term ($\mathbf{U}_{\mu}(\boldsymbol{\eta}, t)$) is determined by velocity fields obtained from a hydrodynamic model. Diffusivity coefficients from the hydrodynamic model can be used to calculate the diffusive term ($\mathbf{U}_{s}(\boldsymbol{\eta}, t)$), however OpenDrift can also estimate the diffiusivity coefficients using in-built parametrizations when the coefficients are not avaiable in the ocean model output. Finally, OpenDrift returns individual (traceable) positions $\boldsymbol{\eta}_{\zeta}[n]$ for each seeded particle at each time-step they spend in the model domain.

https://doi.org/10.5194/egusphere-2025-998
Preprint. Discussion started: 26 March 2025
© Author(s) 2025. CC BY 4.0 License.

2.2.1 Particle mass

To associate the particle distribution with dissolved gas content, we latch a *particle mass* Γ_ζ to each seeded particle, which explicitly corresponds to the number of moles each particle represents (this mass has no influence on the particle buoyancy). Each particle is thus interpreted as a virtual single-point representation of some local spatial distribution of Γ_ζ moles of dissolved gas molecules. Particle mass can be modified at each time-step to simulate processes affecting gas content. Each particle therefore has a successively constructed mass time-series, where the current mass $\Gamma_\zeta[n]$ is determined by the previous mass $\Gamma_\zeta[n-1]$ and one or more mass modification functions $\gamma_\zeta[n-1]$.

The initial mass, i.e. mass at release, of an arbitrary particle ζ seeded at time-step n is scaled such that the total released particle mass approximates the total number of moles of gas dissolved in the water column during a time interval Δt centered on t_n. In practice, we distribute the integrated sum of modeled (using the gas phase model) injected gas molecules from $t_n - \Delta t/2$ to $t_n + \Delta t/2$ evenly over the seeded particles. Assuming seabed flux is stationary within the time interval $t_n \pm \Delta t/2$, we get the initial mass

$$\Gamma_\zeta[n] = \frac{\Delta t \sum_{p=0}^{P} \Upsilon_p[n]}{S[n]} \tag{3}$$

where $\Upsilon_1[n], \Upsilon_2[n], \ldots, \Upsilon_P[n]$ [mol s^{-1}] are total injected dissolved gas from all P modeled seeps.

2.2.2 Particle count

Our framework must be able to model an extensive 3-dimensional domain (e.g. larger ocean regions), making computational complexity a challenge. Both computational time and estimation quality (of "real" conditions) increase with the number of active particles present in the domain. This makes it crucial to be able to strike a decent compromise between the two, which typically involves removal of particles that have been present in the domain for a certain number of time-steps, referred to as particle death. Total particle count $\Lambda[n]$ in the domain can then be expressed as

$$\Lambda[n] = \Lambda[n-1] + S[n] - L[n] - \wp[n], \tag{4}$$

where $L[n]$ is the number of particles leaving the model domain, and $\wp[n]$ the number of dying particles. A constant particle count is obtained when $S[n] \sim L[n] + \wp[n]$. Since $\wp[n]$ represents non-physical loss of gas, the model simulation would ideally run with a spin-up time that ensures $S[n] \sim L[n]$. Unfortunately, this typically results in unreasonable computation times and/or spin-up periods, making particle death necessary. To limit errors caused by dying particles, we implemented a function that redistributes mass from all dying particles to nearby living particles. The redistribution is weighted according to the inverse distance from the dying particle within a user defined distance limit d_{max}, giving a surviving particle s an added mass of

$$\gamma_s = \Gamma_\theta \frac{||\boldsymbol{\eta}_\tau - \boldsymbol{\eta}_\theta||_2^{-1}}{\sum_{\zeta \in \mathcal{T}} ||\boldsymbol{\eta}_\zeta - \boldsymbol{\eta}_\theta||_2^{-1}} \tag{5}$$

from the dying particle θ. Here, $\tau \in \mathcal{T}$ and $\mathcal{T}$ is the set of surviging particle indices ζ satisfying $\|\boldsymbol{\eta}_\zeta - \boldsymbol{\eta}_\theta\|_2 \leq d_{max}$, and $\|\cdot\|_2$ denotes the Euclidean norm. This solution changes the problem of non-physical loss of dissolved gas to one of non-physical redistribution, which is generally considerably less problematic.

https://doi.org/10.5194/egusphere-2025-998
Preprint. Discussion started: 26 March 2025
© Author(s) 2025. CC BY 4.0 License.

2.3 Grid Projected Adaptive-bandwidth Kernel Density Estimator

Having an explicit relationship between dissolved gas content (of seep origin) and particle mass Γ_ζ allows us to infer gas concentrations by evaluating the particle mass per unit volume, which we refer to as the particle density. Let us assume that the particles $\zeta = 0, 1, 2, ..., Z$ are scaled/weighted (by their mass Γ_ζ) samples from an unknown, smooth, underlying particle density field $\phi(x, y, z, t)$ which approximates the seep-induced gas concentration anomaly field $\Phi'(x, y, z, t)$. Estimation of $\Phi'(x, y, z, t)$ can then be done via the estimate $\widehat{\phi}$ of $\phi(x, y, z, t)$ using the particle data set.

To get $\widehat{\phi}$, we employ a discrete spatiotemporal grid $[i, j, k, n]$, where $i = 1, 2, .., I$, $j = 1, 2, .., J$, $k = 1, 2, ..K$, $n = 0, 1, 2, .., N$, and I, J, K, N denote the number of grid cells in east, north, vertical and temporal dimensions, respectively. Grid cell center positions are given by $[x_i, y_j, z_k, t_n]$, with horizontal resolution $\Delta\lambda$ (in both directions), vertical resolution Δz, and temporal resolution Δt. We then bin all mass in the temporal and vertical domains and obtain separate estimates $\widehat{\phi}[i, j]$ of $\phi(x_i, y_j)$ for each resulting depth layer k and time-step n to form the final estimate $\widehat{\phi}[i, j, k, n]$. Obtaining $\widehat{\phi}[i, j, k, n]$ thus translates to solving a series of 2-dimensional density estimation problems (see e.g. Silverman, 1986).

Due to the extensive model domain and the fact that we obtain one estimate for every depth layer and time-step ($K \times N$ estimates), our density estimator needs to be fast and allow reliable density estimates from limited particle counts. The histogram estimator is a simple and extensively used solution in similar situations, however, we found it unsuitable for our application because of its wasteful information exploitation and improper handling of low concentration regions (the histogram estimator and its drawbacks are detailed in Appendix B). Instead, we formulated a new 2-dimensional adaptive Kernel Density Estimator (KDE) to provide our density estimates.

Kernel density estimation is a standard non-parametric way to estimate the density of a random variable using kernel functions (Silverman, 1986). This offers a density estimate that is differentiable, grid cell size independent and often more realistic compared to the histogram estimator, without lower density limitations. For particle dispersion model output data, this involves placing a symmetric, smooth, and, in our case, weighted kernel function at each particle position. By summing up the functions, the density field $\widehat{\phi}$ at position $\boldsymbol{r}_0$ can then be estimated via the general kernel density estimator formula:

$$\widehat{\phi}(\boldsymbol{r}_0) = \frac{1}{V} \sum_{\zeta=1}^{Z} \Gamma_\zeta K_h \left(||\boldsymbol{r}_0 - \boldsymbol{\eta}_\zeta||_2 \right). \tag{6}$$

Here, $K_h(\xi) \equiv (1/h) K(\xi/h)$, where $K(\xi)$ is a non-negative, normalized, and symmetric kernel function, h a bandwidth (smoothing) parameter, and $\boldsymbol{r}_0$ the estimate position.

It is well established that the choice of kernel shape $K(\xi)$ is of less importance, as long as it adheres to the kernel function requirements. We define the base kernel $K(\xi)$ as a standardized 2-dimensional Gaussian, i.e. $K(\xi) = \exp\left(-\xi^2/2\right)/2\pi$. This kernel choice is consistent with our interpretation of particles representing a host of CH_4 molecules and the macroscopic outcome of the diffusive term in the trajectory generator (Eq. (2)).

Selecting an appropriate bandwidth h is crucial, as a poor choice can cause large errors (De Haan, 1999), particularly due to over-smoothing (Larsen et al., 2002). Several methods exist for selecting h by evaluating the statistical properties of the collected data, but they typically rely on strict assumptions on the underlying field. Additionally, for heterogeneous fields (as

https://doi.org/10.5194/egusphere-2025-998
Preprint. Discussion started: 26 March 2025
© Author(s) 2025. CC BY 4.0 License.

in our case) where the statistical properties vary across the domain, local adaptation of h is necessary to give realistic density estimates in both high and low particle count areas. Our domain also includes complex boundaries in the form of bathymetry and coastlines. These aspects also pose a challenge with computational complexity. Our proposed KDE is bathymetry bounded and estimates a locally adapted h using an expanded version of Silverman's rule (Silverman, 1986) which accommodates correlated, weighted data and handles computational complexity via grid-projection and pre-computation of kernels. Testing and validation of the estimator were done using synthetic simulations (see Appendix C).

2.3.1 Grid projection and pre-computed kernels

To improve computational times, we have implemented a grid-projected estimator (Sole-Mari et al., 2019). This involves obtaining a preliminary density $\tilde{\phi}[i,j]$ using the histogram estimator via Eq. (B1), i.e. calculate the accumulated particle mass of all particles within each grid cell. All mass now belongs to a discrete grid, where any difference in position $\mathbf{r}$ between two locations of interest $[i,j]$ and $[i_0,j_0]$ can be expressed as $(i-i_0, j-j_0)\Delta\lambda$.

Furthermore, we pre-compute a set normalized kernels with fixed, discrete bandwidths given by:

$$h[\omega] = \frac{\omega\Delta\lambda}{3}, \quad \text{where} \quad \omega = 0,1,2,...\Omega. \tag{7}$$

Each initial non-discrete bandwidth estimate h' from the data-driven bandwidth algorithm is then mapped to the nearest candidate in $h[\omega]$. Kernel support is set to $\pm\omega\Delta\lambda$ beyond which the kernel contribution is set to zero. Leaked kernel mass is added back across the kernel domain using the Kernel function. These simplifications make complexity scale with particle containing cells instead of particles. It also allows for fast vectorized operations which drastically reduce computation time and results in negligible errors for large grids (Sole-Mari et al., 2019).

2.3.2 Data-driven adaptive bandwidth selector

The conventional Silverman's rule of thumb (Silverman, 1986) selects the optimal bandwidth h that minimizes the integrated mean square error under the assumption of Gaussian distributed data with variance σ^2. For a d-dimensional Gaussian kernel, one obtains

$$h = \left(\frac{4}{d+2}\right)^{\frac{1}{d+4}} N^{-\frac{1}{d+4}}\sigma, \tag{8}$$

where N is the number of data samples, i.e., the number of particles. For $d=2$, the expression simplifies to

$$h = N^{-\frac{1}{6}}\sigma. \tag{9}$$

Here we modify Silverman's rule to yield reasonable estimates for our multi-modal, correlated, non-homogeneous, weighted data set by: i) adapting h locally for a square shaped horizontal "adaptation" grid of size $P \times P$ surrounding each particle containing grid cell, ii) estimating the *effective* (uncorrelated) sample size N_{eff} and iii) implementing bias corrections to a σ-estimator for weighted data-sets. The size P is determined by an integral length scale estimate (as outlined below) of the

https://doi.org/10.5194/egusphere-2025-998
Preprint. Discussion started: 26 March 2025
© Author(s) 2025. CC BY 4.0 License.

entire $I \times J$ 2-d grid. For an arbitrary cell $[i, j]$, the adaptation grid is defined by letting l and m be discrete indices on the grid such that $1 \leq l, m \leq P$ with step size $\Delta\lambda$ in both directions. The number of particles contained in the local grid (prior to grid projection) is denoted as N_g, and the pre-computed histogram density $\tilde{\phi}$ serves as the underlying data for obtaining estimates of the local h. We will now describe the procedure of obtaining estimates of N_{eff} and σ to get the local h for an arbitrary adaptation grid.

Spatial correlations present in environmental data decrease the effective degrees of freedom in the sample set and we must therefore estimate and use the effective sample size N_{eff} to obtain a reasonable h for the local grid (e.g. Larsen et al., 2002). To estimate the effective number of spatially uncorrelated samples, a measure of correlation length is employed. We use the so-called *integral length scale* known from turbulence theory and statistical physics, see e.g., (Yaglom, 1987; Frisch, 1995; Pécseli, 2000) as our objective measure of the correlation length. The correlation length L_c in terms of the integral length scale is formally defined by Frisch (1995)

$$L_c = \frac{\int_0^\infty |R(\varrho)| d\varrho}{R(0)}, \tag{10}$$

where $R(\varrho) = \mathbb{E}\{\phi(x)\phi(x+\varrho)\}$ is the spatial autocorrelation function (ACF) of a continuous univariate spatial random process $\phi(x)$, ϱ is a spatial lag coordinate, and $\mathbb{E}\{\cdot\}$ is the statistical expectation operator.

We now proceed by defining a *local integral length* scale L_c for the binned adaptation window. First, we estimate the local one-dimensional ACF of $\tilde{\phi}$ along each row l and column m of the square grid by using the standard unbiased ACF estimator (e.g., Percival & Walden, 1993)

$$\widehat{R}_l^{row}[\lambda] = \frac{1}{P-\lambda} \sum_{m=1}^{P-\lambda} \tilde{\phi}_{l,m} \tilde{\phi}_{l,m+\lambda} \qquad \text{for} \quad l = 1, 2, ..., P \tag{11}$$

$$\widehat{R}_m^{col}[\lambda] = \frac{1}{P-\lambda} \sum_{l=1}^{P-\lambda} \tilde{\phi}_{l,m} \tilde{\phi}_{l+\lambda,m} \qquad \text{for} \quad m = 1, 2, ..., P \tag{12}$$

where $\tilde{\phi}_{l,m}$ is the binned particle density in grid cell $[l, m]$ and $\lambda = 0, 1, , ..., P-1$ is the discrete horizontal spatial lag index. Assuming local spatial homogeneity, we then arithmetically average the ACF estimates over all P rows and columns, respectively, to yield two one-dimensional ACF estimates as

$$\widehat{R}^{row}[\lambda] = \frac{1}{P} \sum_{l=1}^{P} \widehat{R}_l^{row}[\lambda] \quad \text{and} \quad \widehat{R}^{col}[\lambda] = \frac{1}{P} \sum_{m=1}^{P} \widehat{R}_m^{col}[\lambda]. \tag{13}$$

We now assume local spatial isotropy and let the arithmetic average of the two perpendicular ACFs serve as a representative single ACF for the adaptation window

$$\widehat{R}[\lambda] = \frac{1}{2} \left(\widehat{R}^{row}[\lambda] + \widehat{R}^{col}[\lambda] \right). \tag{14}$$

https://doi.org/10.5194/egusphere-2025-998
Preprint. Discussion started: 26 March 2025
© Author(s) 2025. CC BY 4.0 License.

Using the estimated ACF, we can finally estimate the local one-dimensional integral length scale $\widehat{L}_c$ for the adaptation window by discretizing Eq. (10) as

$$\widehat{L}_c = \frac{\sum_{\lambda=0}^{P-1} |\widehat{R}[\lambda]| \Delta\lambda}{\widehat{R}[0]}. \tag{15}$$

We now express the correlation length in terms of the associated number of samples as $N_c = \widehat{L}_c/\Delta\lambda$. It is easy to show that $1 \leq N_c \leq P$. We then define the number of effectively uncorrelated particles N_{eff} as

$$N_{\text{eff}} = \frac{N_g}{N_c}, \tag{16}$$

and it directly follows that $N_g/P \leq N_{\text{eff}} \leq N_g$. The interpretation of N_{eff} is straightforward: if all particles are spatially uncorrelated, then $N_{\text{eff}} = N_g$, and if all particles are fully correlated (e.g., if they are all trapped in a coherent structure), then N_{eff} attains its lower limit $N_{\text{eff}} = N_g/P$.

To obtain an estimate $\widehat{\sigma^2}$ of the variance σ^2 in the two-dimensional binned data, we need to account for the loss of degrees of freedom due to shortening of the residual vector (Bessel's correction) and weighting as well as increased variance due to the binning process itself. The estimate of variance for the binned particle density $\tilde{\phi}_{l,m}$, can then be expressed as

$$\widehat{\sigma^2} = \left(\frac{\sum_{l,m} \tilde{\phi}_{l,m} \|\mathbf{r}_{l,m} - \boldsymbol{\mu}\|_2^2}{\sum_{l,m} \tilde{\phi}_{l,m}} \right) \left(\frac{1}{1-\mathcal{B}} \right) + \sigma_b^2, \tag{17}$$

where $\mathbf{r}_{l,m}$ denotes the grid cell center point position vectors, $\sum_{l,m} \equiv \sum_{l=1}^{P} \sum_{m=1}^{P}$, and

$$\boldsymbol{\mu} = \frac{\sum_{l,m} \tilde{\phi}_{l,m} \mathbf{r}_{l,m}}{\sum_{l,m} \tilde{\phi}_{l,m}} \tag{18}$$

is the weighted mean position vector, and $\left(\frac{1}{1-\mathcal{B}}\right)$, where

$$\mathcal{B} = \frac{\sum_{l,m} \tilde{\phi}_{l,m}^2}{\left(\sum_{l,m} \tilde{\phi}_{l,m}\right)^2}, \tag{19}$$

is a bias correction term that accounts for Bessel's correction and the reduced degrees of freedom due to uneven sample weights (Kish, 1965, pp 86-88). The variance increase due to the binning process (Sheppard's correction, see e.g. Vardeman, 2005) is included through the correction term $\sigma_b^2 = \Delta\lambda^2/12$.

The final local bandwidth estimate then follows from Eq. (9):

$$\widehat{h} = N_{\text{eff}}^{-\frac{1}{6}} \widehat{\sigma}. \tag{20}$$

2.3.3 Boundary solution

We establish a boundary solution for the density estimator by interpolating bathymetry data onto the model grid across all predefined depth layers, creating a matrix of "permissible" and "impermissible" cells for gas. The boundary control is imposed

https://doi.org/10.5194/egusphere-2025-998
Preprint. Discussion started: 26 March 2025
© Author(s) 2025. CC BY 4.0 License.

at the kernel estimation stage before summation, by directly modifying kernels whose support contains impermissible cells (see Figure 2). While being computationally intensive, this greatly simplifies the boundary control and entirely omits the difficulties of finding a reliable boundary solution that handles the complex bathymetry and physical processes appropriately.

Impermissible cells are treated as impenetrable obstacles, and any density within, or "blocked" by impermissible cells, is considered misplaced. A cell is defined as blocked if it lacks a clear line of sight to the kernel center. We determine line of sight using Bresenham's line algorithm (Bresenham, 1965). This is an efficient incremental algorithm relying solely on integer arithmetics that identify grid cells located between an origin cell (x_0, y_0) and a target cell (x_1, y_1) (Figure 2). The algorithm is implemented on a normalized grid with unit cell lengths and initialized by first defining the direction, or step coefficients sx and sy in the x and y directions, respectively:

$$\mathrm{sx} = \begin{cases} 1, & \text{if } x_0 < x_1 \\ -1, & \text{if } x_0 > x_1 \end{cases}, \quad \mathrm{sy} = \begin{cases} 1, & \text{if } y_0 < y_1, \\ -1, & \text{if } y_0 > y_1. \end{cases}, \tag{21}$$

and an error term $\varepsilon = \mathrm{dx} - \mathrm{dy}$, where $\mathrm{dx} = |x_1 - x_0|$ and $\mathrm{dy} = |y_1 - y_0|$. The algorithm then iteratively updates (x_0, y_0), using ε to determine whether to step in x or y direction (sx, sy are not updated) via the following criteria:

$$2\varepsilon > -\mathrm{dy}: \quad x_0 \Rightarrow x_0 + sx \quad \text{and} \quad 2\varepsilon < \mathrm{dx}: \quad y_0 \Rightarrow y_0 + sy. \tag{22}$$

At each time step, (x_0, y_0) is added to the list of grid cells, thereby iteratively forming the line of sight to the target cell. Density in blocked or impermissible cells are redistributed to permissible cells according to the kernel function.

2.4 Atmospheric flux and mass modification functions

Changes in dissolved gas content due to processes within or at the boundaries of the water column are included by modifying the particle mass. Total mass change is estimated for each time-step n and particle ζ using predefined mass modification functions. Here, our modeling framework is relatively flexible, and can even accommodate models where it is necessary to keep track of higher order parameters, such as microbe stocks (e.g. a Monod model). This is made possible since we can model any parameter explicitly across the domain (although this will increase computation time). We will only describe mass modification due to dissolved atmospheric exchange of gas here, but a mass modification function for microbial oxidation of CH_4 is presented in the application section (Sect 3).

Atmospheric flux can be implemented following any theory using the surface layer concentration as input data. Here we propose a simple solution by applying the bulk equation from Wanninkhof (2014):

$$F = \kappa\left(\Phi_{atm} - \Phi_{sw}\right), \tag{23}$$

where F [mol m^{-2} s^{-1}] is the gas flux across the sea-air interface, κ [m s^{-1}] is the gas transfer velocity, and Φ_{atm} and Φ_{sw} [mol m^{-3}] are atmospheric and surface water concentrations, respectively. The gas transfer velocity κ can be expressed as

$$\kappa(U_a, T_s) = C_\kappa U_a^2 \left(\frac{Sc(T_s)}{660}\right)^{-1/2}, \tag{24}$$

https://doi.org/10.5194/egusphere-2025-998
Preprint. Discussion started: 26 March 2025
© Author(s) 2025. CC BY 4.0 License.

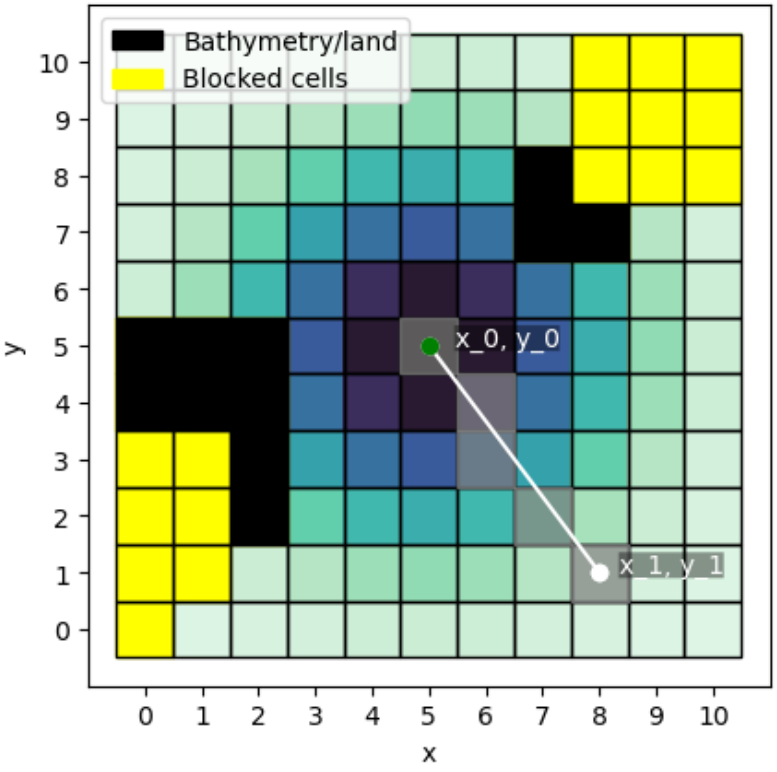

Figure 2. Sample kernel with support $i, j = 0, 1, ..., 10$, containing impermissible cells in its kernel support. Density is indicated by blue shading and impermissible cells (Bathymetry/land) and blocked cells where mass from the shown kernel is not permitted to access are shown as black and yellow colored cells, respectively. Cells identified as being in the line of sight between the kernel center (green dot) and cell $[1, 8]$, according to Bresenham's line algorithm, are grayed out (although there is nothing particular about this line).

where $Sc(T_s)$ and C_κ are empirically derived constants and U_a is the surface wind speed. The Schmidt number $Sc(T_s)$ is an empirically derived, gas-specific temperature-dependent dimensionless constant describing the fractional relationship of kinematic water viscosity to the diffusion coefficient of the gas. The C_κ coefficient lumps together a set of various processes that govern sea/air exchange and was determined for CO_2 only, using inverse modeling for global estimates and a wind speed range of $4 < u_a < 15$ m s^{-1}. Validity for other gases and wind ranges is not fully known.

Let the gridded estimate of the 2-d spatiotemporal atmospheric flux field $\beta(x, y, t)$ be denoted $\widehat{\beta}[i, j, n]$, using the same horizontal and temporal grid cells as $\widehat{\phi}[i, j, k, n]$. We then assume an initial equilibrium between the atmospheric concentration and background surface concentration, which is disturbed by the (modeled) seep-derived dissolved gas. The difference between surface water and atmospheric concentration in Eq. (23) is then simply the surface layer ($k = 0$) concentration $\widehat{\phi}[i, j, 0, n]$. To obtain an estimate of the gas transfer coefficient κ, we project re-analysis atmospheric wind and sea surface temperature data onto all i, j, and ns, delivering the gridded gas transfer coefficient field estimate $\widehat{\kappa}[i, j, n]$. The gridded atmospheric dissolved

https://doi.org/10.5194/egusphere-2025-998
Preprint. Discussion started: 26 March 2025
© Author(s) 2025. CC BY 4.0 License.

flux field estimate is then given by

$$\widehat{\beta}[i,j,n] = \widehat{\kappa}[i,j,n]\,\widehat{\phi}[i,j,0,n]\,\Delta\lambda^2\Delta t, \tag{25}$$

where $\widehat{\beta}[i,j,n]$ is the integrated atmospheric flux from grid cell $[i,j,n]$.

Loss of gas due to atmospheric flux is implemented by modifying the particle mass of all particles present in the surface layer. Since the atmospheric flux function varies linearly with the dissolved gas content, the mass adjustment can be implemented by distributing loss (at any given time-step) according to the contribution from each particle to the total atmospheric flux. This is done via a weighted mean calculation, i.e. the mass modification term for atmospheric loss at time-step n for a particular surface layer particle a is given by

$$\gamma_a[n] = \frac{\Gamma_a[n]}{\sum_{\zeta\in\mathcal{A}}\Gamma_\zeta[n]} \sum_{i=1}^{I}\sum_{j=1}^{J}\beta[i,j,n] \tag{26}$$

where $a \in \mathcal{A}$ and $\mathcal{A}$ denotes the set of indices for all particles in the surface layer and $\gamma_a[n]$ is mass loss to the atmosphere.

3 Application

We applied the modeling framework to a well documented natural CH_4 seep site offshore northwestern Norway located in the Hola trough (Figure 3), where coral reefs and CH_4 seeps coexist (Chand et al., 2008). These seeps were studied not only for assessing and investigating mechanisms governing atmospheric fluxes, but also for their potential impact on local cold water coral reefs. A thorough description of the data, environmental conditions, and the seabed flux estimation are presented in Ferré et al. (2024). In essence, the seeps are weak, hence we focus here on examining the dynamics and fractional distribution of the gas rather than actual environmental impact of the current conditions in the area.

We modeled the 45 CH_4 seeps observed at this site and the resulting direct and diffusive atmospheric gas release as well as 3D concentration fields for the period between May 20 and June 20, 2018. A 1-month period was chosen since it captures a relatively wide range of periodic variability in both ocean and atmospheric circulation patterns and yields relatively modest computation times. The OpenDrift simulation required 2-3 days on a supercomputer and the concentration modeling 5-6 hours on a workstation laptop.

3.1 Seep gas phase modeling

Steady state free and dissolved gas profiles and direct free atmospheric gas flux were modeled individually for each of the 45 seeps using M2PG1 (see Sect. 2.1) to steady state, using observed and inferred input data and settings, as outlined in the following sections.

3.1.1 Gas phase modeling input data and settings

Temperature and salinity data were extracted from a Conductivity Temperature Depth (CTD) cast performed in May 20, 2018 (Figure 3 and 4a). Seabed gas fluxes for each of the $P = 45$ individual seeps were estimated using single beam echosounder

https://doi.org/10.5194/egusphere-2025-998
Preprint. Discussion started: 26 March 2025
© Author(s) 2025. CC BY 4.0 License.

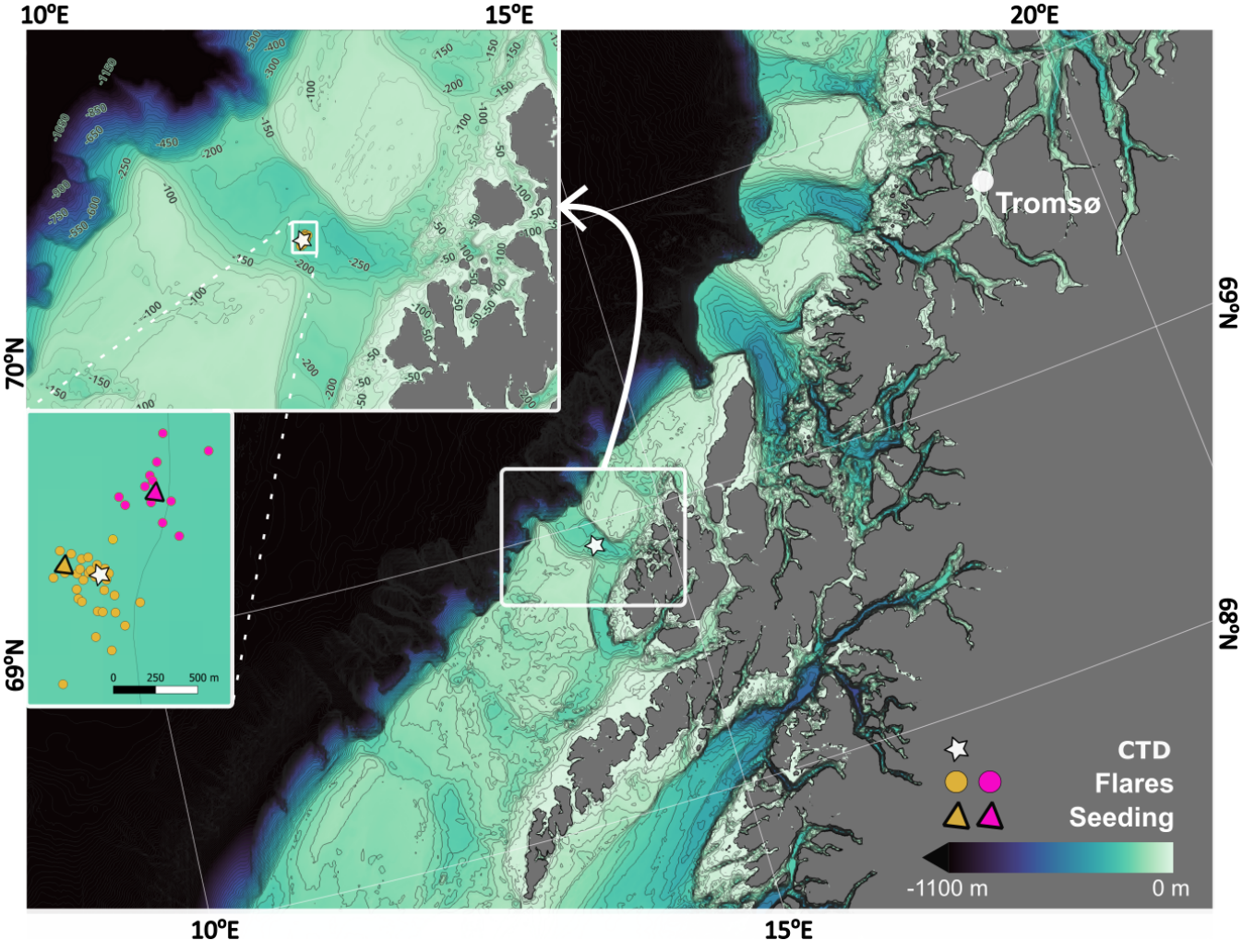

Figure 3. Bathymetric map of the application area and location of Conductivity Temperature Depth (CTD) station, observed seep-associated flares indicated by yellow and pink dots during the May 20-22, 2018 survey. Seeding locations (where particles in the particle trajectory model is released), estimated as the flux weighted average position of the incorporated seeps, are indicated by the yellow and pink triangle (see chapter 3.2). Coloring reflects which seeding location each seep observation is pooled into.

https://doi.org/10.5194/egusphere-2025-998
Preprint. Discussion started: 26 March 2025
© Author(s) 2025. CC BY 4.0 License.

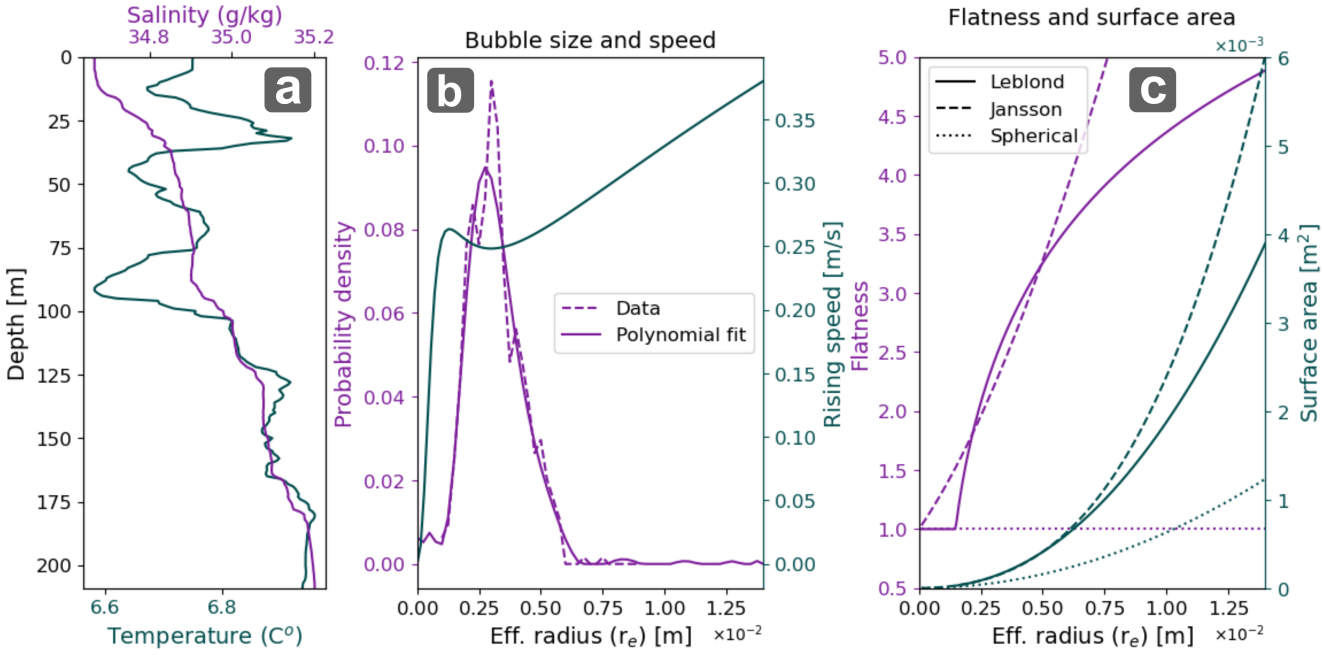

Figure 4. Input parameters used in the M2PG1 model runs. a) Conservative temperature and absolute salinity (at the CTD station obtained in May 20, 2018 b) Bubble size distribution (Veloso et al., 2015) and bubble rising speed (Fan and Tsuchiya, 1990) for different bubble sizes as a function of effective radius $r_E = (a^2 b)^{1/3}$ c) Bubble flatness and surface area for various bubble sizes as function of effective radius for Jansson et al. (2019), Leblond et al. (2014), and Spherical flatness parametrization. Note that the linear flatness (Jansson flatness) appears non-linear in the figure since its linearity is with major spheroid axis and not effective radius.

data (Simrad EK-60 scientific SBE splitbeam echosounder) obtained between May 20 and May 22 2018 as presented in Ferré et al., 2024. All other input parameters had to be inferred as outlined in the following paragraphs since we lack observations.

M2PG1 requires an initial bubble size distribution, and we used the polynomial fit to visual observations as presented in (Veloso et al., 2015). Note that since M2PG1 takes into account the non-spherical shape of bubbles, the bubble size distribution is given using the effective radius $r_E = (a^2 b)^{1/3}$, where a and b are the major and minor axis of the spheroid, respectively (Figure 4b). We used the bubble rising speed model from Fan & Tsuchiya, (1990) using their recommendation for bubble contamination and the linear flatness parametrization from Jansson et al., (2019) (see Figure 4 b and c). We describe and discuss the bubble rising speed model and deformation parametrization selection in Appendix D.

Horizontal domain size was determined using A and an assumed barotropic current of $\overline{U} = 0.1$ m s^{-1}, horizontal diffusivity $D_h = 0.01$ m^2 s^{-1}, rising speed $\langle w \rangle = 0.25$ m s^{-1} and a $H = 200$ m deep water column. We estimated σ_w using the bubble rise spectrum (Figure 5) to $\sigma_w = 0.025$ m s^{-1}. This resulted in an estimated model area of $A_{\mathcal{M}} \sim 88$ m^2 and grid cell side-lengths 9.4 m. Vertical and temporal resolution does not affect grid cell concentrations but must obey the Courant-Friedrichs-Lewy condition. Here we use a grid cell height of 1 m to obtain $A^{\perp}_{\mathcal{M}} = 9.4$ m^2 and a time-step of 0.0625 s. In addition to

https://doi.org/10.5194/egusphere-2025-998
Preprint. Discussion started: 26 March 2025
© Author(s) 2025. CC BY 4.0 License.

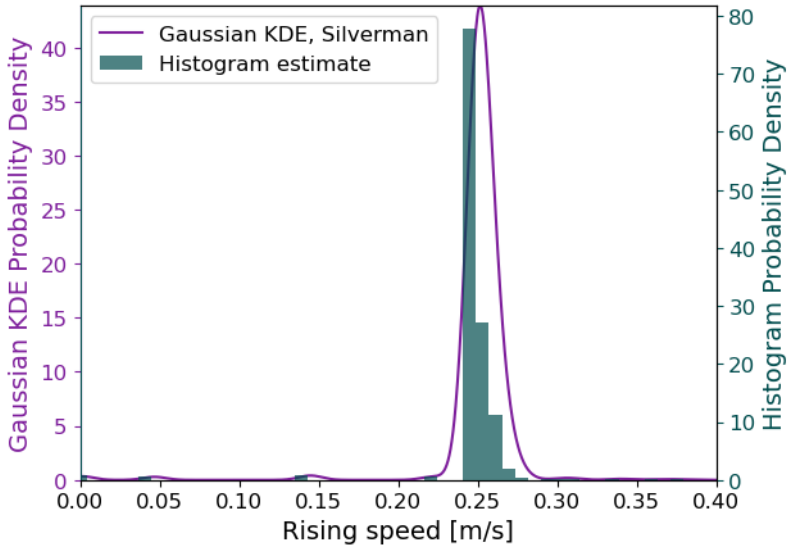

Figure 5. Probability density for bubble rising speed of bubbles in the bubble plume using the bubble rising speed model from Fan and Tsuchiya (1990) and bubble size distribution from Veloso et al. (2015).

the assumptions outlined above, we assumed a constant vertical mixing coefficient of $D_v = 0.001$ m^2 s^{-1} and background dissolved gas concentrations were set to the default values from Jansson et al., (2019) $6.8 \cdot 10^{-4}$mol l^{-1}, $2.5 \cdot 10^{-4}$mol l^{-1}, $2.5 \cdot 10^{-5}$ mol l^{-1}, $2 \cdot 10^{-9}$ mol l^{-1} and $1.5 \cdot 10^{-8}$ mol l^{-1} for N_2, O_2, CO_2, CH_4, and Ar, respectively.

We provide an overview of microbial oxidation rate coefficient (k_{ox}) used in the literature and their associated uncertainty in Appendix E and Figure 6. Here we use an average rate coefficient of $k_{ox} = 3.6 \cdot 10^{-7}$ s^{-1} based on the compiled dataset (Table E1), which includes observations from seep environments, hydrothermal vents, and human-made releases.

3.1.2 Gas phase modeling results

Most CH_4 gas is dissolved in the water column, with concentration exponentially decreasing towards the sea surface (Figure 7a). Hourly seabed gas flow rate was ~ 97 moles of which 93% dissolved below 100 m depth and only $\sim 0.28\%$ reaching the atmosphere. Integrated atmospheric release from free gas over the 1-month period was 183.1 moles. Free CH_4 gas content closely follows the total free gas content throughout the water column (Figure 7a) and loss of total free gas volume (bubble shrinkage, collapse, and dissolution) dominates over other gases replacing CH_4 in bubbles. The resulting change in dissolved gas profiles for the four other gases (N_2, O_2, CO_2 and Ar) due to bubble transit, i.e. the transport of gas molecules by entering bubbles, rising, and subsequently dissolving at shallower depths, was therefore negligible (never exceeding 0.1% of background values). Atmospheric flux from the 45 seeps varied considerably from $< 10^{-7}$ to $\sim 10^{-5}$ (Figure 7c), mostly due to large variations in seabed fluxes (Ferré et al., 2024). Dissolved gas injection rates, which is needed as input in the particle dispersion

https://doi.org/10.5194/egusphere-2025-998
Preprint. Discussion started: 26 March 2025
© Author(s) 2025. CC BY 4.0 License.

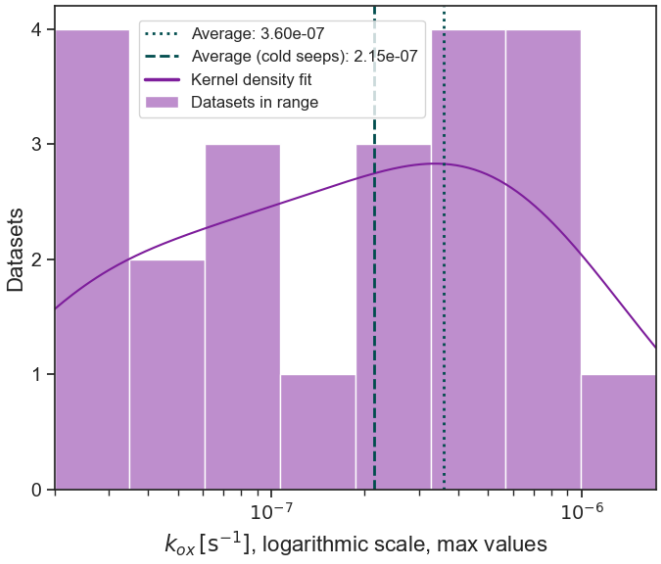

Figure 6. Maximum CH_4 oxidation rate coefficients (k_{ox}) obtained from datasets found in literature and detailed in E and Table E1. The x-axis is logarithmic, meaning that the bars cover different ranges, i.e. the histogram bars are narrower at smaller scales.

modeling step, were calculated using the dissolved gas profiles (not shown) and Eq. (1) and are shown for the 45 seeps in Figure 8a.

3.2 Particle data set

Using OpenDrift, we simulated a particle data set of $\zeta = 1, 2, 3, N$ particles with associated 4D-positions (3D space and time) for the 1-month period, as described in Sect. 2.2.

The advective and diffusive components for the drift model (Eq. 2) were determined using velocity vectors and diffusivity coefficients (throughout the water column) obtained from the NorKyst-800 hydrodynamic modeling system. NorKyst-800 is based on the Regional Ocean Modeling System (ROMS, Shchepetkin & McWilliams, (2005)) framework. It is a terrain-following, free-surface, primitive equations model with 35 terrain-following vertical layers and a horizontal resolution of 800m (Albretsen et al., 2011). The model is eddy-permitting and can resolve major fjord systems and other coastal bathymetric features such as troughs. Vertical turbulent exchange is computed using the General Length Scale closure scheme (Umlauf and Burchard, 2003). NorKyst is the primary ocean model used by Norwegian authorities for search and rescue and oil spill response planning and is, therefore, the best available ocean model covering our study area (Albretsen et al., 2011). OpenDrift has an option to automatically check if diffusivity coefficients are reasonable from a physical perspective, and we used a non-zero fallback value of $D = 0.2$ $m^2 s^{-1}$ when OpenDrift deemed the input data unphysical. OpenDrift did not excessively use the fallback value, and from tests where we increased and decreased the value, we found that our choice of fallback value had negligible impact on the results.

https://doi.org/10.5194/egusphere-2025-998
Preprint. Discussion started: 26 March 2025
© Author(s) 2025. CC BY 4.0 License.

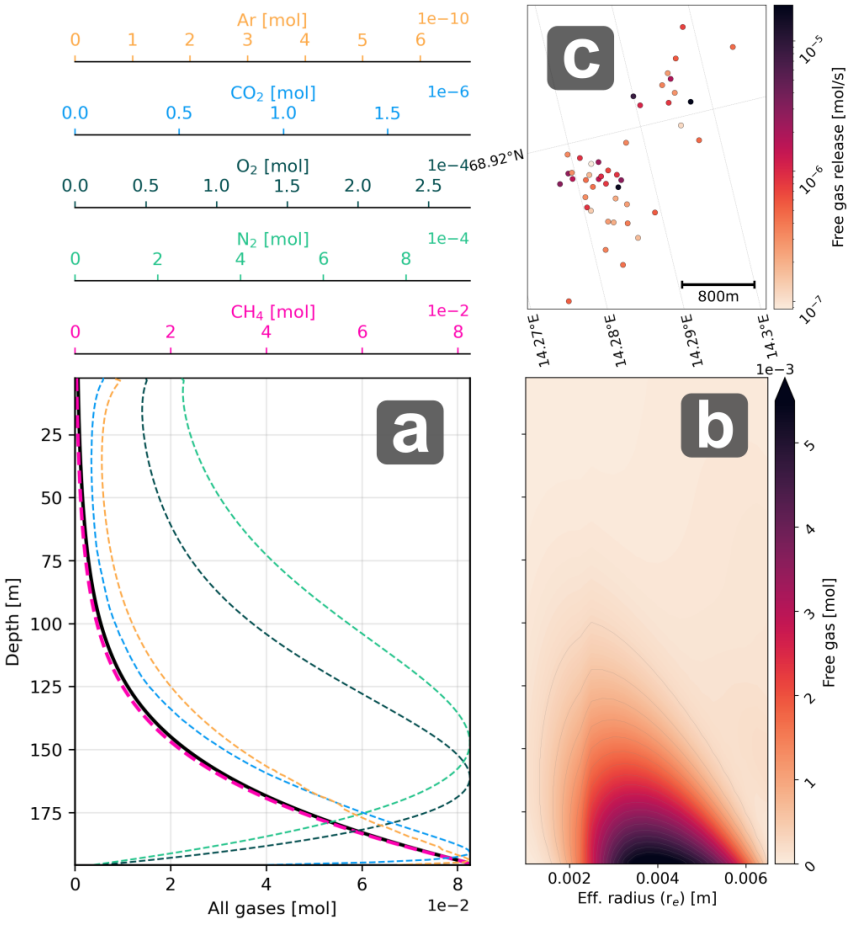

Figure 7. a) Vertical profiles of total free gas content for the 5 gases (colored axes) and the total free gas (black, lower x-axis) in the water column for all seeps combined b) Distribution of gas content on bubble sizes for all seeps and gases combined at different depths (note power in scale) c) Free atmospheric gas flux at the sea surface for the 45 seeps (logarithmic color scale).

https://doi.org/10.5194/egusphere-2025-998
Preprint. Discussion started: 26 March 2025
© Author(s) 2025. CC BY 4.0 License.

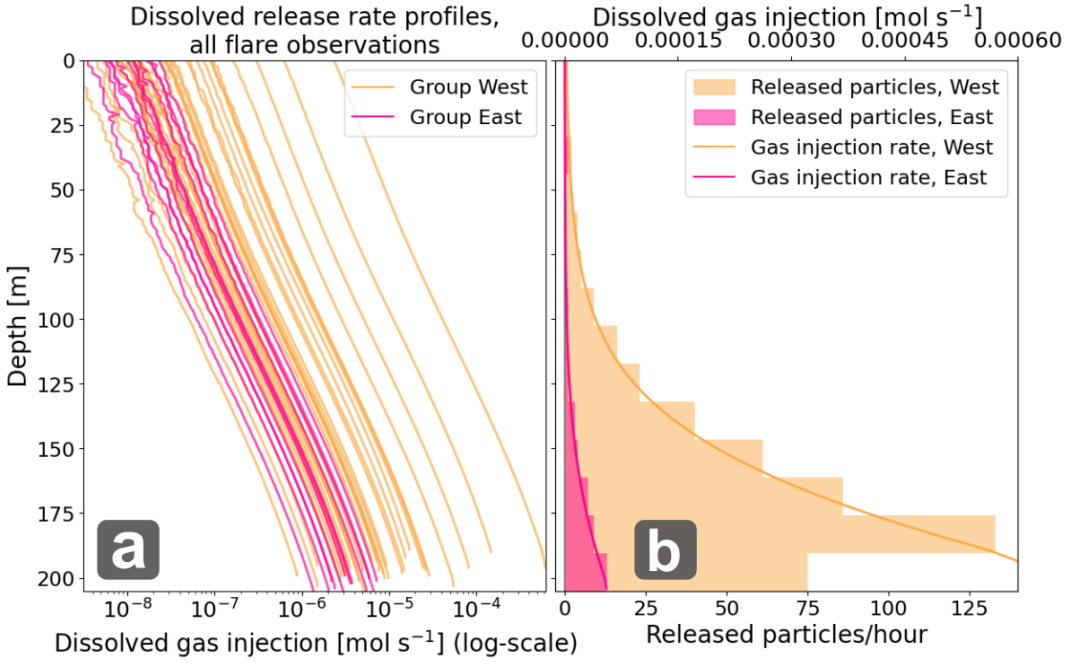

Figure 8. a) Dissolved CH_4 release rate profiles (q_m) for all observed seeps on a logarithmic scale for the two cluster groups (see Figure 3 for seep/group locations, group west in yellow and group East in pink), and b) Resulting accumulated dissolved CH_4 release rate from each groups (lines, upper x-axis) and histogram of released particles at each modeling time-step (hourly). The smaller bottom bar at the western cluster reflects the slightly shallower depth in this area.

We seeded 500 particles every time-step, and set the particle lifetime to 4 weeks. OpenDrift then simulated the particle trajectories by updating their positions every 5 minutes. The effect of vertical mixing on the particle trajectory was modelled using a sub-timestep of 30 seconds. We configured OpenDrift to store the particle positions every full hour during the simulation.

The initial particle mass was calculated using seabed gas flux data and Eq. (3). To saturate the particle field prior to the study period, the simulation and seeding were initiated on April 20 (1-month spin-up time). With this setup, total particle mass in the domain would increase in the first 10-15 days of the study period due to the re-distribution of dying particle mass. However, particle count would remain approximately constant, with $\Lambda \sim 330\ 000$ particles present at each time-step.

Due to the large range in seep intensity and relatively closely clustered seep positions (Figure 7), combined with the limitation of 500 particles each time-step, we chose to aggregate all the seeps into two seeding locations. This was done to promote smooth release profiles and reduce round-off effects. Grouping was done based on visual inspection of the seep positions (Figure 3) and seed locations were calculated using the flux-weighted average position of each group, given by:

$$\mathbf{r} = \frac{\sum_{g \in \mathcal{G}} \Upsilon_g \mathbf{r}_g}{\sum_{g \in \mathcal{G}} \Upsilon_g}, \tag{27}$$

https://doi.org/10.5194/egusphere-2025-998
Preprint. Discussion started: 26 March 2025
© Author(s) 2025. CC BY 4.0 License.

where $\mathcal{G}$ denotes the set of all seep indices included in the seed position. The seed locations and their associated seeps are indicated by matching colored triangles and dots in Figure 3. The 500 particles were then distributed according to the injection rate profiles for each seed location with a 1 m vertical resolution, resulting in the profiles/histograms shown in Figure 8b.

3.3 Concentration and atmospheric flux estimation

Concentration and atmospheric fluxes were estimated on a $[i, j, k, n]$ grid with cell sizes $\Delta\lambda = 800$ m, $\Delta z = 25$ m, and $\Delta t = 3600$ s, covering the time period between May 20 and June 20 and geographical region between (12.5^{o}E, 68.5^{o}N), (12.0^{o}E, 72.1^{o}N), (21^{o}E, 72^{o}N), and (20.1^{o}E, 68.45^{o}N). Although particle data were technically available outside of this region, we chose this boundary to avoid potential edge effects in the hydrodynamic model and to reduce computation time. Kernel bandwidths were estimated for every depth layer using a $P \times P$ sized adaptation grid where we determined P using an integral length scale estimate of every 2-D (i, j) layer of the particle data. The size of P, typically varying between ~ 7000 and ~ 20000 m, agreed reasonably well with observations and theory on meso-scale eddy sizes in the region (Dugstad et al., 2021). Boundary conditions were implemented as described in Sect. 2.3.3 using $[i, j]$- interpolated IBCAO v. 4 bathymetry data (Jakobsson et al., 2012). Spatiotemporal gas transfer velocities $\widehat{\kappa}[i, j, n]$ were estimated from ERA V reanalysis wind and sea surface temperature data (Hersbach et al., 2023) which, together with the surface layer concentration estimates $\widehat{\phi}[i, j, 0, n]$, gave the atmospheric flux field estimates $\widehat{\beta}[i, j, n]$ using Eq. (25).

Particle mass was adjusted at each time-step using the mass modification terms (γ) for atmospheric flux (Eq. 26) and redistribution from dying particles (Eq. 5). We also added a mass modification term for microbial oxidation, a crucial process when simulating the evolution of dissolved CH_4 content in the ocean (Appendix E). We used a simple first order kinetics formula (Eq. E1), with the same rate coefficient $k_{ox} = 3.6 \cdot 10^{-7}$ as in the gas phase model (see Appendix E and Figure 6 for the determination of k_{ox}). Microbial oxidation was then included by imposing a mass modification term $\gamma_{ox} = k_{ox}\Delta t\Gamma_\zeta[n-1]$ at each time-step (individually for every active particle ζ). In principle, this corresponds to discretization of Eq. (E1) using a standard first order forward finite difference scheme.

3.4 Application results

The results from the gas phase modeling step is shown and described in Section 3.1.2 and the dissolved concentrations, atmospheric flux and fate of CH_4 molecules in the modeled domain in the following sections. Animations of the time varying 3-D CH_4 concentration field and 2-D diffusive release field is shown in supplementary material S1 and S2, respectively.

3.4.1 3-D CH_4 concentration field

The averaged distribution pattern of CH_4 throughout the study period is strongly affected by generally northeastward currents that transports gas along the coast, following the shelf and shelf break. The gas enters the more open fjord systems, and to a lesser degree inner fjords. North of 70^o the CH_4 plume disperses more, branching into a northward plume leaving the coast and a coastal plume that keeps following the coastline. The concentration anomaly is generally small, around 2-4 orders of

https://doi.org/10.5194/egusphere-2025-998
Preprint. Discussion started: 26 March 2025
© Author(s) 2025. CC BY 4.0 License.

magnitude lower than typical oceanic CH_4 background concentration values ($\sim 3 \cdot 10^{-6}$mol m^{-3} (Figure 9), given the weak seabed release.

The 3-D concentration field is very dynamic due to the energetic regional current regimes, and shows variability on ranging from tidal (∼12 hours) to fortnightly periods. A visual representation of the temporal variability of the top 9 layers in the water column (down to 200 m depth) is shown in supplementary material S1 (see video supplement section).

Most of the CH_4 is displaced upward relatively quickly from the trough and pushed on top of the shelf break (Figure 9). Vertical distribution of CH_4 is therefore characterized by a quick (a few days) shift from exponentially increasing towards the seafloor to increasing towards the sea surface after release (Figure 10). A thorough analysis of mechanisms causing the rapid shift in location of CH_4 is outside the scope of this study, however, upwelling within troughs and along the shelf break is well documented in this region (e.g. Slagstad et al., 1999).

3.4.2 Diffusive CH_4 flux to the atmosphere

The total time-integrated 2-D distribution of diffusive atmospheric CH_4 release for the study period and the model domain is shown in Figure 11 and the complete time series can be found in supplementary material S2 (see Video supplement section). Within the model domain, most of the CH_4 remains in the water column or is consumed by microbes, with a total of ∼0.76% (∼528 moles) being exchanged diffusively with the atmosphere. This is ∼3 times the total free gas release ($\sim 0.3\%$) and does not account for any diffusive release occurring outside of the model domain. The diffusive release extends across a large ocean region covering hundreds of kilometers and exhibits high temporal variability, strongly correlated with wind speed (Figure 13a) via the gas transfer velocity function. However, no clear effect of surface water depletion is observed after storm events. Microbial consumption exceeds atmospheric flux by a factor of ∼20 - ∼100 (Figure 13b), mainly driven by regional wind speeds and, consequently, atmospheric diffusive flux. Loss from the domain due to particles leaving is also substantial (∼5 to ∼50 times the atmospheric loss) and shows clear tidal excursions patterns with periodic variability (Figure 13c). Non-physical methane loss due to dying isolated particles (i.e. too far away to be re-distribution) is on the same order of magnitude as loss to the atmosphere via diffusive release (Figure 13d).

3.4.3 Fate of released CH_4

Excluding deactivated particles and CH_4 leaving the model domain, the accumulated fractional water column loss due to atmospheric exchange shows an exponential increase the first 2-3 days, with a subsequent near linear slope until the end of the study period, reaching a loss of $\sim 0.7\%$ after the particle lifetime of 4 weeks (Figures 12a and b). The short period of exponential increase fits well with the rapid vertical shift in the position of dissolved CH_4 in the water column occurring over the first week after release (Figure 10). Methane lost to microbial oxidation greatly exceeds the diffusive and free gas atmospheric flux, and $\sim 65\%$ is consumed after 1 month (~ 63 times the total atmospheric release from free and dissolved fluxes combined). Since microbial decay dominates, it also closely follows the logarithmic solution of the decay rate function (Eq. E1). All loss combined means that ∼34 % of the CH_4 remains in the water column after 1 month.

https://doi.org/10.5194/egusphere-2025-998
Preprint. Discussion started: 26 March 2025
© Author(s) 2025. CC BY 4.0 License.

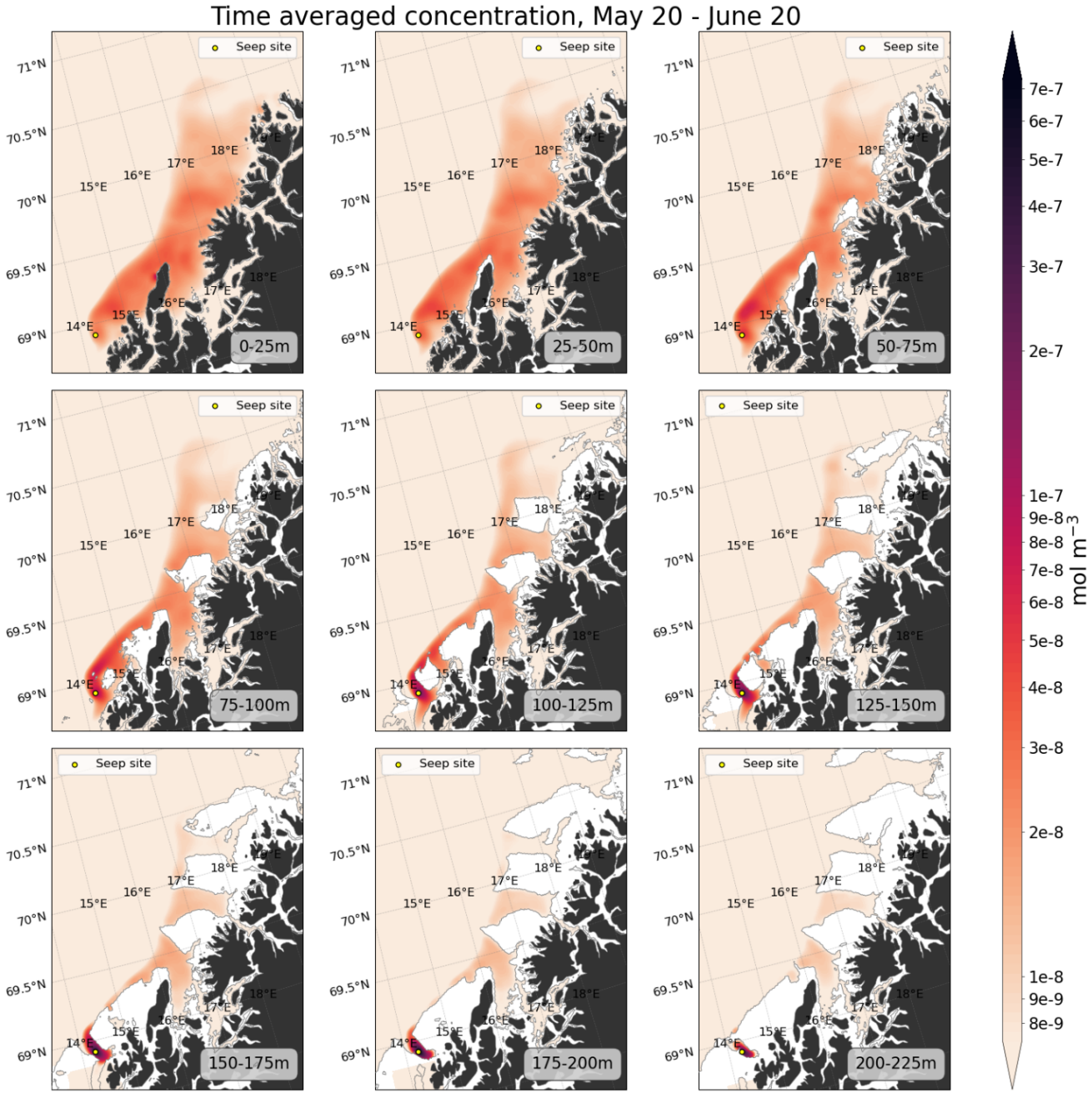

Figure 9. Four depth layers of modification to the CH_4 concentration on May 1 as indicated on top of each panel. Typical background concentration in the ocean is $\sim 3 \cdot 10^{-6}$mol m^{-3} for reference. The bathymetric boundary for the different layers are delineated with a grey contourline.

https://doi.org/10.5194/egusphere-2025-998
Preprint. Discussion started: 26 March 2025
© Author(s) 2025. CC BY 4.0 License.

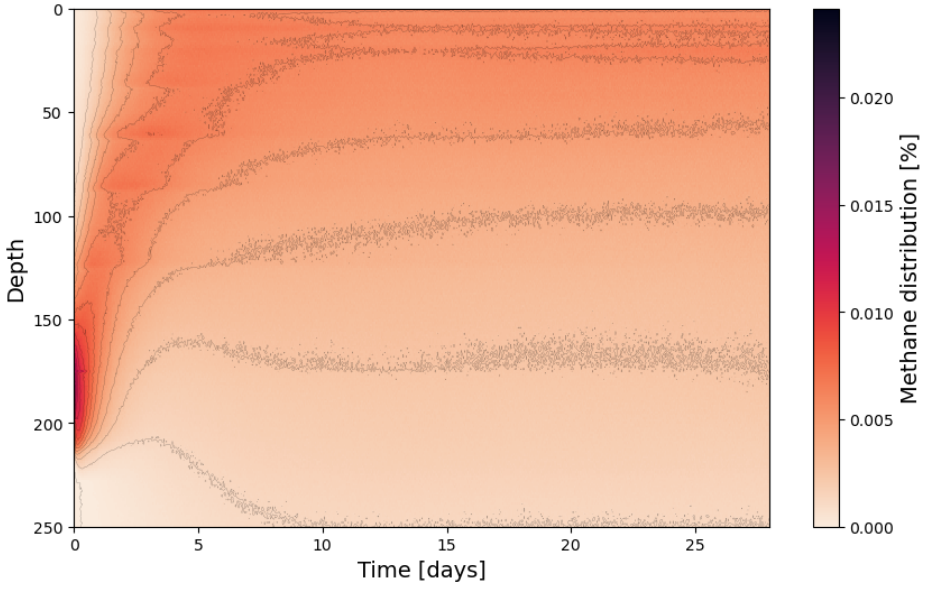

Figure 10. Fractional vertical distribution of CH_4 in the water column 28 days after release. Color scale shows the fraction of total depth integrated CH_4 in the water column.

3.4.4 Interpretation of results

Diffusive exchange of CH_4 exceeds the local free gas release and spreads over a large ocean region, making it almost impossible to detect and quantify using conventional measuring instrument. It also poses a challenge for atmospheric inversion models, since these are better at detecting point sources rather than weak releases over large regions (Thompson and Stohl, 2014). This highlights the uncertainty in quantifying the impact of seabed seepage on the atmospheric CH_4 budget, in particular when considering the potential increased seepage in recent decades due to e.g. thawing marine permafrost, hydrate dissociation (e.g. Serov et al., 2015; Ruppel and Kessler, 2017), and physical interventions into the seafloor by humankind (e.g. drilling). Although here the estimated total atmospheric flux is small, the impact of more extensive seepage such as the vast seepage region along the West Spitsbergen continental margin (Mau et al., 2017) could be significant and at the same time difficult to observe and/or trace.

Even though the dissolved gas spreads out over cold water coral reef areas, the CO_2 generated by microbial oxidation is too small to have any noticeable affect on the local ocean environment and cold water corals. This is primarily due to the weak seabed release. For more intense and/or localized seepage, e.g. a leaking gas well, this might not be the case.

A major caveat, both regarding atmospheric fluxes and potential impact on the ocean environment, is the uncertainty concerning the microbial oxidation rate coefficient k_{ox} and atmospheric flux bulk model. Observations of k_{ox} vary by several orders of magnitude, corresponding to half-lives ranging from 5 days to almost 2 years (Figure 6, Table E1). The atmospheric gas transfer coefficient function (Eq. (24)) was derived based on, and designed for global CO_2 estimates (Wanninkhof, 2014)

https://doi.org/10.5194/egusphere-2025-998
Preprint. Discussion started: 26 March 2025
© Author(s) 2025. CC BY 4.0 License.

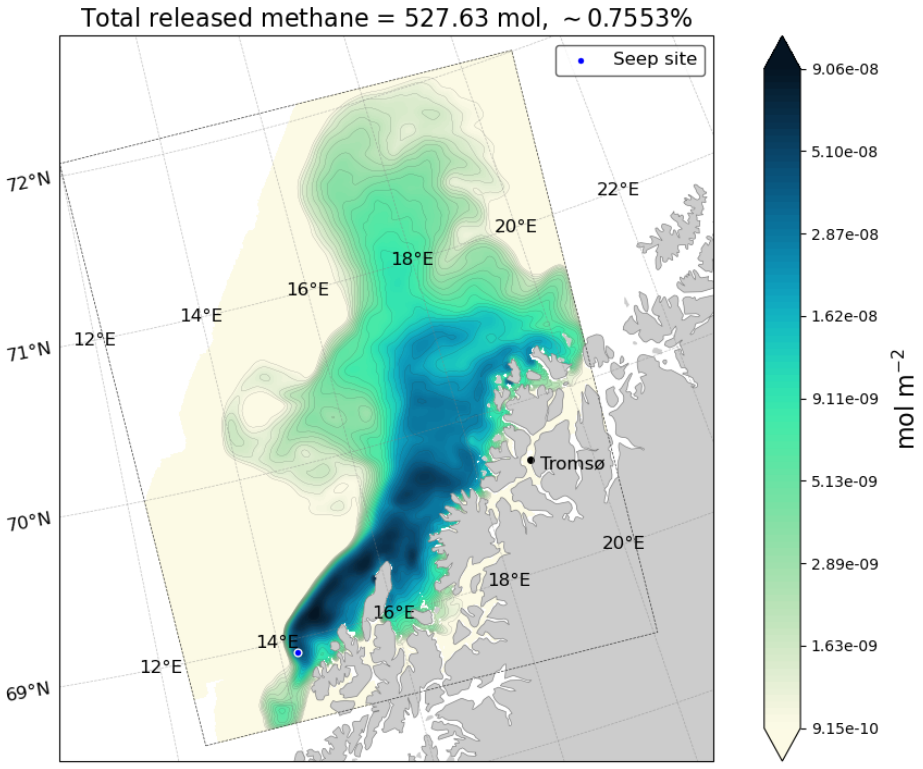

Figure 11. Modeled accumulated diffusive release of CH_4 within the model domain from the seeps between May 20 and June 20, 2018.

and has an estimated uncertainty of $\sim 20\%$, even for its intended use. We must expect considerably higher uncertainties due to our application in a local coastal region (as opposed to an ocean basin), where wind speeds may exceed the validity range, and since the specific coefficient C_κ has been determined solely for CO_2. Improving the microbial oxidation and diffusive exchange modules are keys to provide more realistic modeling of the fate of dissolved CH_4 in the future.

4 Conclusions

We implemented and successfully applied a new framework for modeling the impact of seabed gas seepage on spatiotemporal water column concentrations and atmospheric gas exchange with the ocean. The application uncovered and highlighted important aspects of the dynamics regarding the fate of seeped gas from the seabed, such as a highly distributed diffusive release which considerably exceeds local free atmospheric gas fluxes.

The main challenges with the current framework are high uncertainty in the atmospheric flux module and in the mass modification modules. Our results are also sensitive to poorly resolved diffusivity coefficients, which can greatly affect the water column distribution of dissolved gas. A steady state assumption for the seepage itself might also be a problematic assumption in areas where seepage is known to vary strongly over time (e.g. Ferre et al., 2020).

https://doi.org/10.5194/egusphere-2025-998
Preprint. Discussion started: 26 March 2025
© Author(s) 2025. CC BY 4.0 License.

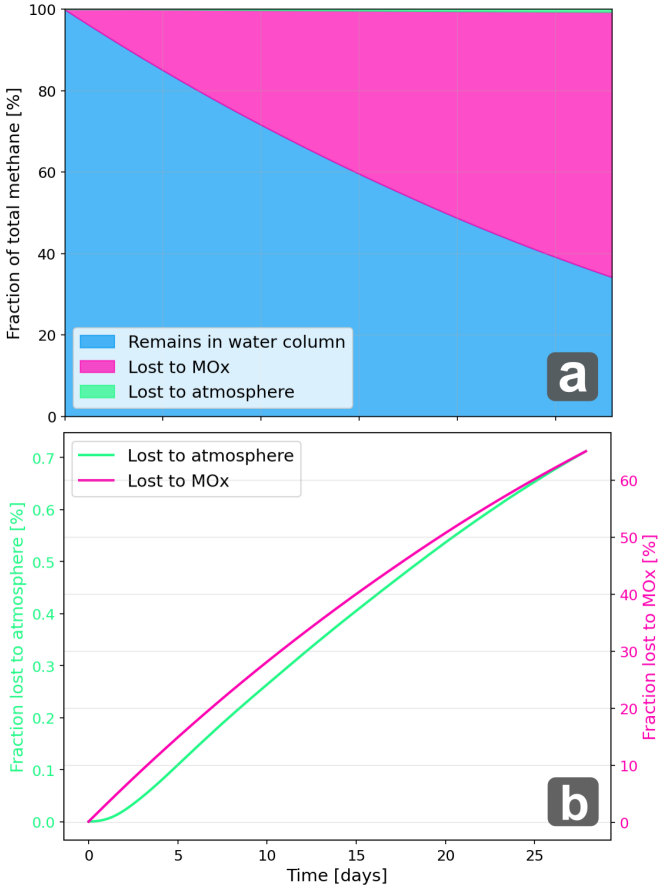

Figure 12. a) Accumulated fractional loss to atmospheric exchange and microbial oxidation and fraction CH_4 that remains in the water column and b) Accumulated fractional loss to atmospheric exchange and microbial oxidation in days after release.

From a pure modeling perspective, non-physical re-distribution of dissolved gas is also a source for potential error and when estimating the final fate of gas, the limitation in model domain size makes inference about final state difficult. Using a steady state solution of the gas phase model is also a drawback and might currently cause significant errors, especially for intense seep sites where background gas concentrations can be significantly altered.

The framework is flexible and reasonably fast and makes it possible to employ complex, locally adapted existing hydrodynamic models as well as customizable process modules, thereby capturing not only idealized processes but also complex hydrodynamic and chemical/biological phenomena. Thus, it provides a considerable improvement on previous attempts to model the fate of dissolved gases in the water column (e.g. Graves et al., 2015). It has a wide range of potential applications, not only for monitoring known gas seeps, but also for risk assessments concerning future potential increased seepage due to e.g. hydrate thawing, James et al., 2016, leaking gas wells, and integrity of subsea legacy carbon storage reservoirs (e.g. Torsæter et al., 2024) and other leaking industrial installations. Aspects of the framework (e.g. the kernel density estimator) can also be

https://doi.org/10.5194/egusphere-2025-998
Preprint. Discussion started: 26 March 2025
© Author(s) 2025. CC BY 4.0 License.

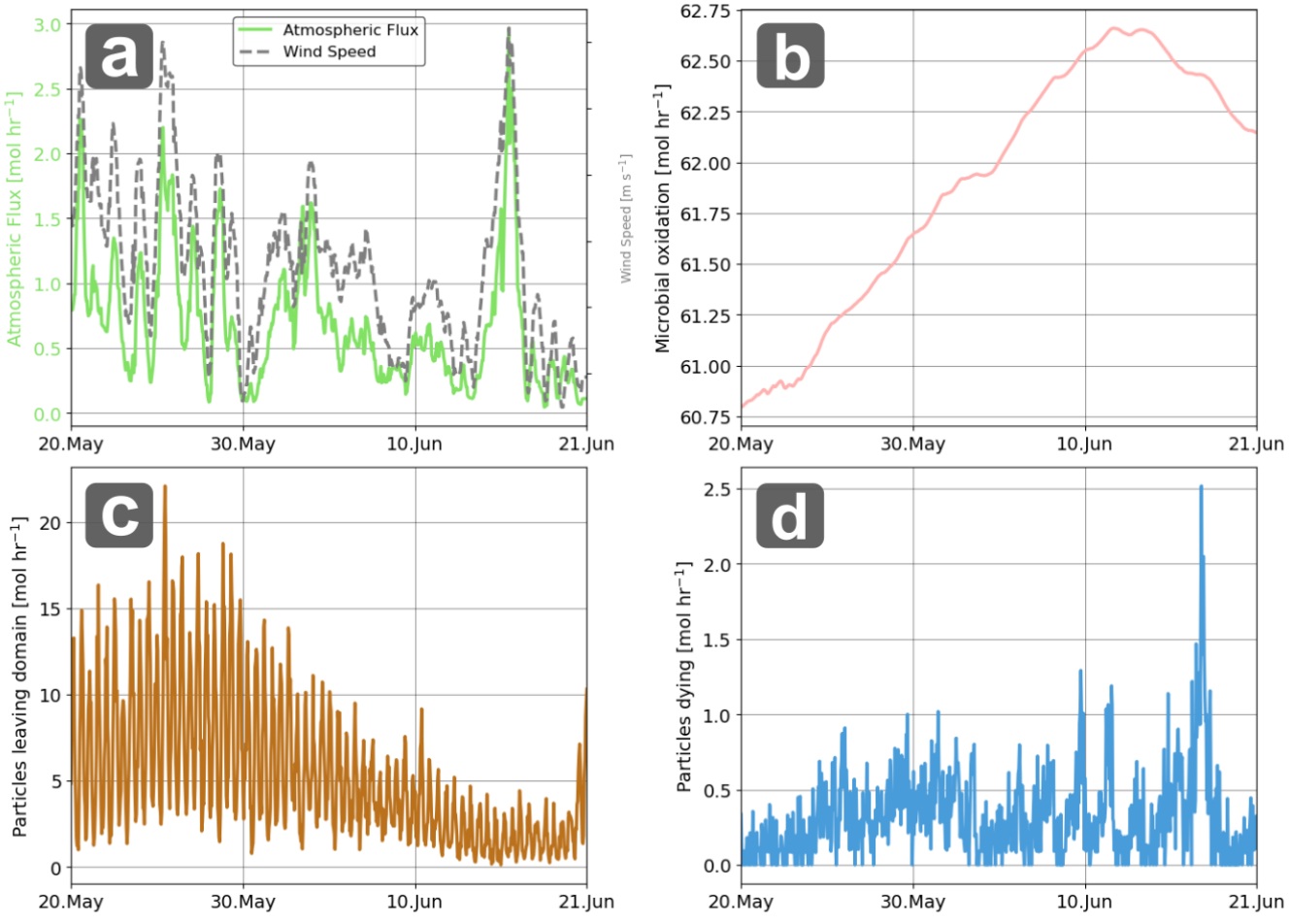

Figure 13. a) Loss of CH_4 from the water column from atmospheric equilibrium, b) Microbial oxidation, c) Particles leaving the model domain and d) Mass loss due to deactivation of particles that are unable to redistribute its mass.

complementary to established frameworks for post-processing and analysis of ocean particle dispersion data and contaminant spreading in the ocean in general (e.g. the ChemicalDrift module, Aghito et al., 2023). Aside from improving process and atmospheric exchange modules, future developments should consider a full on-line coupling between concentration model and gas phase model as well as a proper validation study to ensure realistic results.

Code and data availability. Code for creating input data to and output data from M2PG1 as well as running the model in batch for multiple seeps can be found at DOI: 10.5281/zenodo.15042452 or GitHub. The adaptive kernel density estimator and testing of the adaptive kernel density estimator can be accessed at DOI: 10.5281/zenodo.15042426 or GitHub and the code for the whole framework, as well as seed

https://doi.org/10.5194/egusphere-2025-998
Preprint. Discussion started: 26 March 2025
© Author(s) 2025. CC BY 4.0 License.

profiles, including the code used for running OpenDrift can be accessed at DOI: 10.5281/zenodo.15042437 or at GitHub. The particle position output data from the OpenDrift model run can be accessed at DOI: 10.5281/zenodo.15042308.

Video supplement. Supplementary material 1 (SI1) can be accessed at DOI: 10.5446/69942 and supplementary material 2 (SI2) can be accessed at DOI 10.5446/69941.

Appendix A: M2PG1 Model Grid Cell Dimensions

Here we propose a solution for determining a reasonable horizontal model grid cell size assumption for M2PG1, as no established method currently exist. Since M2PG1 assumes horizontally invariant concentrations within the predefined model domain, the choice of the horizontal model domain size directly affects the concentration within the model grid cells and, in turn, gas transfer and dissolution. Defining the horizontal dimensions of the model grid cells must therefore be done with care and should reflect the horizontal extent of the modeled bubble plume to obtain realistic results. We determine the horizontal and vertical gas phase model grid cell area, respectively denoted $A_{\mathcal{M}}$ and $A^{\perp}_{\mathcal{M}}$, by modeling the 2-dimensional spread of the bubble cloud.

We assume that the seeps are point sources and that the bubbles drift with a barotropic current with mean speed $\overline{U}$ and random velocity fluctuations governed by a horizontal diffusivity D_h. In this framework, horizontal bubble spread is caused by i) differences in accumulated horizontal displacement resulting from varying rising speeds of bubbles with different sizes (slow/fast bubbles spend more/less time in the velocity field) and ii) turbulent (random) effects in the horizontal flow, modeled as diffusion. The horizontal extent of the bubble plume increases towards the sea surface and we use the estimated spread at half of the total water column depth H to minimize estimation errors at the surface/bottom.

The spread due to differences in rising speed can be estimated using the probability density P for bubble rising speeds w_o in the bubble cloud. The distribution of rising speeds for bubbles in the bubble cloud can be described by the discrete probability $P[w_o]$, and can be derived from the chosen discrete bubble size distribution (BSD) and bubble rising speed model. This is done by estimating the bubble rising speed of all bubbles in the BSD and re-bin the results, using the fractional weights from the BSD, according to bubble sizes. We obtain the weighted distribution average and standard deviation as

$$\langle w \rangle = \frac{\sum_o w_o P[w_o]}{\sum_o P[w_o]} \quad \text{and} \quad \sigma_w = \sqrt{\frac{\sum_o (w_o - \langle w \rangle)^2 P[w_o]}{\sum_o P[w_o]}}, \tag{A1}$$

where w_o are discrete rising speeds, $P[w[o]]$ associated probabilities, $\langle w \rangle$ the weighted average, and σ_w weighted the standard deviation (see Figure 5 for an example).

Along-flow spread Δx_{rs} can then be expressed as

$$\Delta x_{rs} = \overline{U} \Delta t_{max}, \quad \text{where} \quad \Delta t_{max} = \frac{H}{2} \left[\frac{1}{\langle w \rangle - \sigma_w} - \frac{1}{\langle w \rangle + \sigma_w} \right]. \tag{A2}$$

https://doi.org/10.5194/egusphere-2025-998
Preprint. Discussion started: 26 March 2025
© Author(s) 2025. CC BY 4.0 License.

Horizontal displacement due to current diffusivity acts in both along-flow (x) and cross-flow (y) direction and can be expressed by the 2-dimensional Gaussian solution to the diffusion equation for a point source,

$$p(x,y,t) = \frac{1}{\sqrt{4\pi D_h t}} e^{-(x^2+y^2)/4D_h t}, \tag{A3}$$

where $p(x,y,t)$ is the normalized count of bubbles at position (x,y) and time t and $4D_h t$ is the variance of the spread in both directions. We constrain diffusive spread using twice the standard deviation $2\sigma_D$ of the distribution at $H = H/2$ given by

$$\Delta x_D = \Delta y_D = 2\sqrt{2D_h} \cdot \sqrt{0.5 t_H} \quad \text{where} \quad t_H = \frac{H}{\langle w \rangle}. \tag{A4}$$

and

$$A_{\mathcal{M}} = (\Delta x_{rs} + \Delta x_D)\Delta y_D \tag{A5}$$

giving horizontal grid cell side lengths of $\sqrt{A_{\mathcal{M}}}$ (since M2PG1 uses square cells).

An estimate of the vertical grid cell area, which is needed to estimate dissolved gas injection profiles is easily obtained and defined as

$$A^{\perp}_{\mathcal{M}} = \sqrt{A_{\mathcal{M}}}\Delta z_{\mathcal{M}}, \tag{A6}$$

where $z_{\mathcal{M}}$ is the vertical grid cell size.

Appendix B: The histogram estimator

A commonly used density estimator based on data from particle dispersion models is the histogram estimator. The histogram estimator for the concentration estimate $\hat{\phi}$ at position $\boldsymbol{r}_0$ using a predefined grid with grid cell volume V can be expressed as

$$\hat{\phi}(\boldsymbol{r}_0) = \frac{1}{V}\sum_{\zeta=1}^{Z} \Gamma_\zeta K(\boldsymbol{r}_0, \boldsymbol{\eta}_\zeta), \tag{B1}$$

where Γ_ζ and $\boldsymbol{\eta}_\zeta$ represent the mass and positions (respectively) of particles, and

$$K(\boldsymbol{r}_0, \boldsymbol{\eta}_\zeta) = \begin{cases} 1 & \text{when } \boldsymbol{\eta}_\zeta \text{ shares the same grid cell as } \boldsymbol{r}_0, \\ 0 & \text{otherwise.} \end{cases} \tag{B2}$$

Using the histogram estimator implies modeling a smooth, continuously distributed property with a discontinuous, quantized, and piece-wise function, which introduces several drawbacks with this estimator-property pairing. Firstly, the estimator is highly dependent on the choice of grid cell size: fine grids result in noisy and unrealistic estimates in regions with medium to low particle counts, while coarse grids lead to significant loss of information in areas with high particle counts. Secondly, the histogram estimator is highly sensitive to the chosen position of the origin. In addition, the minimum concentration estimate is limited to one particle per grid cell, which can significantly influence e.g. atmospheric flux estimates (for instance if that

https://doi.org/10.5194/egusphere-2025-998
Preprint. Discussion started: 26 March 2025
© Author(s) 2025. CC BY 4.0 License.

concentration exceeds the atmospheric background concentration). Some of these issues can be mitigated by adjusting the grid cell size, however, the problems prevail in highly heterogeneous domains containing regions with low particle saturation (unless one adobts an unstructured grid). Seeding more particles is always a remedy, however, we are still left with inefficient use of the particle position data and potentially unfeasible computational complexity (see Sect. 2.2.2). We have therefore formulated an adaptive bandwidth, 2-dimensional grid-projected Kernel Density Estimator (KDE) specifically for OpenDrift output data to calculate the concentration field.

Appendix C: Density estimator testing and validation

The adaptive kernel density estimator was therefore developed, tested, and compared with other estimators using a numerical toy model that generates data resembling typical OpenDrift data. The toy model gives full control of all parameters and allows to efficiently test various scenarios due to the low computational cost of each run. Here we compare the adaptive bandwidth KDE against three other estimators as explained below.

C1 Toy model and test simulation

The synthetic data was designed to mimic output data from OpenDrift by seeding $N = 1900000$ particles onto a regular 2D grid with indices and size given by $(i, j) \in \mathcal{Z}^{100\times100}$. The position $\mathbf{r}[t_T] = (x[t_T], y[t_T])$ of each particle at time t_T was determined by

$$\mathbf{r}(t_T) = \sum_{t=t_0}^{t_T} \left\{ \mathbf{U}[t_\vartheta] + \sqrt{2D}\boldsymbol{\xi}[t_\vartheta] \right\}, \tag{C1}$$

where $\mathbf{U}[t_\vartheta] = [u(t_\vartheta), v(t_\vartheta)]$ represents a spatially uniform, time varying velocity field, and $\vartheta = 0, 1, 2, 3, ...T$ and t_0 is the seed time for the particle. The stochastic velocity component is determined by $\boldsymbol{\xi}[t_\vartheta]$ which is a vector of independent random numbers sampled from a standard normal distribution $\mathcal{N}(0, 1)$ and D, which is the diffusivity. The velocity field $\mathbf{U}[t_\vartheta]$ is modeled as

$$\mathbf{U}[t_\vartheta] = \frac{\mathbf{U_0} + \boldsymbol{\Xi}[t_\vartheta]}{\|\mathbf{U_0} + \boldsymbol{\Xi}[t_\vartheta]\|} \|\mathbf{U_0}\| \tag{C2}$$

where $\mathbf{U_0} = (u_0, v_0)$ gives the initial velocity, $\Xi[t_\vartheta] = (\sin[\frac{t_\vartheta}{50}]u_0, v_0)$ is a wave component and $||\cdot||$ gives the euclidean norm. The normalization with $\|\mathbf{U}_0\|$ is necessary to ensure conservation of mass in the field. We choose $U_0 = (0.1, 0)$ and $D = 0.14$ and released a total of 10^6 particles from a point source at $\mathbf{r}_0 = (10, 10)$ over the course of 380 timesteps. The normalized histogram density estimate (Eq. B1) of the full simulation was considered the simulation "Ground-truth" and is shown in Figure C1.

C2 Testing and evaluation of different estimators

We implemented and tested four estimators i) The histogram estimator, ii) An Time-dependent bandwidth estimator, iii) The Silverman bandwidth estimator from the *gaussian_kde* function from the *scipy.kde* python package, and iv) The adaptive

https://doi.org/10.5194/egusphere-2025-998
Preprint. Discussion started: 26 March 2025
© Author(s) 2025. CC BY 4.0 License.

bandwidth estimator used in the present study. All estimators were tested on a data set where we picked every 1000th particle from the full dataset (resulting in a total of 1000 particles). All estimates were done grid-projected as described in Sect. 2.3.1 and for the final time-step only and all particles had a mass of 1.

For the histogram estimator estimate, we used Eq. (B1) and for the time-varying bandwidth estimator, we defined the bandwidth as

$$h_{tv} = \sqrt{4Dt_\vartheta} \tag{C3}$$

which is the theoretically ideal bandwidth for the time-varying estimate. In a real-world scenario, the diffusion coefficient varies and we cannot estimate the correct diffusion coefficient unless information about the local diffusivity is given from the hydrodynamic model. Although the bandwidth function could be suitable when such information is available, complex bathymetry may introduce challenges as discussed below. For the estimate using the provided *scipy.kde.gaussian_kde*, we used default settings and the *bw_method='silverman'* setting (SciPy Community, 2024). We refer to the package documentation for details (URL in the reference list). For the adaptive bandwidth estimator, we followed the algorithm described in Sect. 2.3.2 and estimated h locally for each particle-containing grid cell. For the "in-house" coded estimators (all but *scipy.kde.gaussian*) we included the boundary control explained in Section 2.3.3.

A comparison of the four estimators and a residual analysis plot are shown in Figure C2. We have chosen to compare the estimators visually and evaluating how the max values in the field aligns as well as a simple R^2 statistic. The Histogram estimator gives a noisy result, with very high max values of 8000 compared to 5664 for the ground truth. and a low $R^2 = 0.52$. The the non-adaptive Silverman results in an unrealistically smooth estimate, with a very low maximum value of 878 and low $R^2 = 0.55$. While the time varying bandwidth estimator works relatively well in the open "unbounded" part of the domain, it over-smooths when encountering the boundary - highlighting a problem with time varying bandwidth in bounded domains where the stochastic process is limited by physical obstacles. Nonetheless, it performs better than the non-adaptive Silverman and Histogram estimators, achieving an $R^2 = 0.66$. The adaptive bandwidth estimator is in general slightly over-smooth, however, it significantly outperforms the three other estimators with a maximum value of 3692, which is the closest to the ground truth and an $R^2 = 0.87$ (Figure C2 performs well.

Appendix D: Rising speed model and flatness parametrization

It is well-known that the terminal bubble rise veloocity U_b varies non-linearly with the bubble size (e.g., (Fan and Tsuchiya, 1990),(Leifer and Patro, 2002)). In addition, it depends on fluid and gas parameters, and the degree of contamination. Fan and Tsuchiya (1990, Eq. (2.11)) showed that the terminal bubble rise velocity can be written as

$$U_b = \left(U_{b1}^{-c} + U_{b2}^{-c}\right)^{-1/c}, \tag{D1}$$

where U_{b1} dominates for small bubbles, and U_{b2} dominates for large bubbles. The dimensionless parameter c (called n in (Fan and Tsuchiya, 1990) and d in (Leifer and Patro, 2002)) is a measure of the degree of contamination, which directly affects

https://doi.org/10.5194/egusphere-2025-998
Preprint. Discussion started: 26 March 2025
© Author(s) 2025. CC BY 4.0 License.

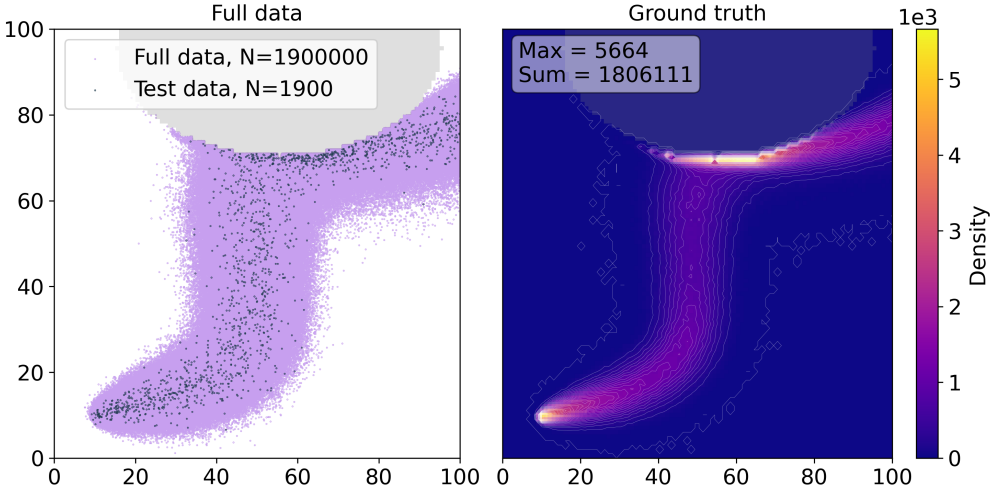

Figure C1. Left: Synthetically generated particle dispersion model data for 1,900,000 particles (purple) and randomly picked "test data" of 1900 particles (green dots) in a domain with a simple "impermissible" elliptic boundary. Right: Histogram estimate of the full 1,900,000 particle dataset, representing the "ground truth" in the test scenario for the adaptive kernel density estimator.

the surface tension of the bubbles. By fitting Eq. (D1) to multiple experimental data sets, Fan and Tsuchiya (1990) found that $0.8 \leq c \leq 1.6$, where the lower limit corresponds to contaminated bubbles, and the upper limits corresponds to clean bubbles. We follow their recommendation, and apply $c = 1.2$ for our assumed moderately contaminated conditions, see Figure 4b and Jansson et al., (2019) for further details.

Bubble deformation is an important factor in bubble dissolution and exchange rates of gas since it changes the surface area to volume ratio of the bubbles. Deformation can be characterized by a dimensionless flatness ratio, defined as $f \equiv a/b$. In addition to spherical flatness, two parametrization options are available in M2PG1: Leblond flatness (Leblond et al., 2014), where $f = 0.45 + 1.4 \ln(a/b_{ref})$ for $a > 1.48$ and Jansson flatness (Jansson et al., 2019), where $f = 1 + 0.3064(a/b_{ref})$ (coined here, referred to as "linear flatness" in Jansson et al., 2019) and $b_{ref} = 1$ mm. While Jansson flatness parametrization has support for bubbles where $a < 1.48$ mm, it lacks an empirical basis other than a fair agreement with Leblond for relatively small bubbles. The divergence between the two models at larger bubble sizes (Figure 4c) can lead to misrepresentations when modeling distributions that are skewed towards larger bubbles. Nonetheless, we use Jansson flatness parametrization since here our observations indicate that most of the gas is confined to smaller bubble sizes (Ferré et al., 2024).

Appendix E: Brief review of existing estimates of MOx rate coefficients

Oxidation of CH_4 to carbon dioxide is achieved by several groups of aerobic methanotrophs and reaction rates vary substantially, depending on existing microbial consortia, stoichiometry of the involving nutrients, and overall succession of the methanotrophs (Hanson & Hanson, 1996). Nonetheless, reaction rate measurements with radiotracer assays highlight first-order

https://doi.org/10.5194/egusphere-2025-998
Preprint. Discussion started: 26 March 2025
© Author(s) 2025. CC BY 4.0 License.

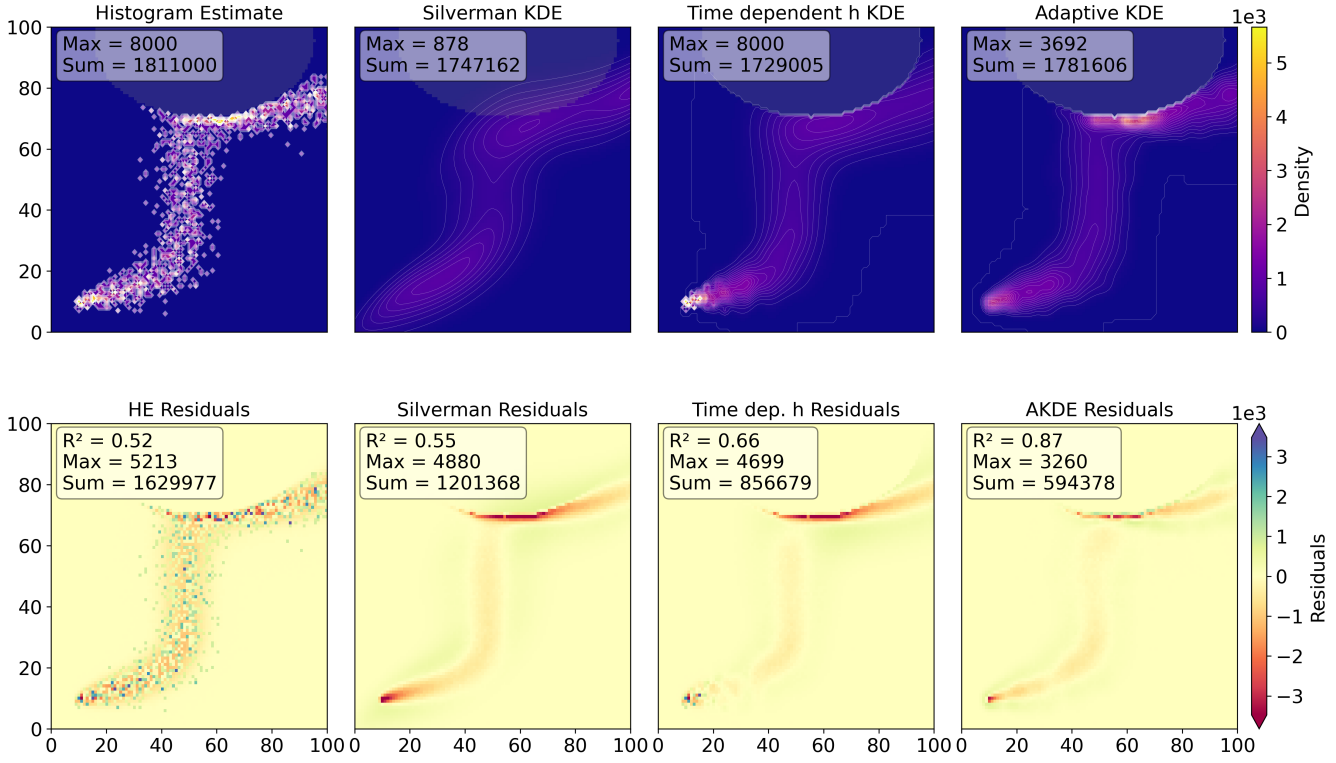

Figure C2. Density estimates using the Histogram estimate of the full simulation (10^6 particles), Histogram estimator, Adaptive bandwidth estimator (AKDE), Adaptive bandwidth estimator (AKDE) with boundary control, Time-dependent bandwidth estimator (TKDE) with boundary control, and the Silverman (non-adaptive) estimator from the *scipy.kde* package. The impermissible region (land/bathymetry) is shaded in grey.

reaction kinetics and a CH_4 decay rate following

$$\frac{d\phi(t)}{dt} = -k_{ox}\phi(t) \quad \Rightarrow \quad \phi(t) = \phi_0 e^{-k_{ox}t} \tag{E1}$$

where k_{ox} is the reaction rate and $\phi_0 = \phi(0)$ the initial concentration. Most measurements of microbial CH_4 oxidation (MOx) in marine environments are focused on locations where CH_4 concentrations exceed the background levels. The rates of CH_4 oxidation in suboxic zones, hydrothermal vents, and cold seeps exhibit substantial variability, spanning several orders of magnitude from 10^{-8} to 10^{-2} nM s^{-1}, primarily due to spatiotemporal fluctuations in CH_4 concentrations. In contrast, half-life or CH_4 oxidation rate constants (k_{ox}) are independent of CH_4 concentration and provide a more accurate representation of the water column's MOx capacity. The rate coefficients (k_{ox}) range from $0.02{\cdot}10^{-6}$ to $1.74{\cdot}10^{-6}$ s^{-1}, corresponding to halving times of approximately five days to two years. However, CH_4 can remain stable for decades in oxygen-limited environments where aerobic CH_4 oxidation is inhibited.

https://doi.org/10.5194/egusphere-2025-998
Preprint. Discussion started: 26 March 2025
© Author(s) 2025. CC BY 4.0 License.

Author contributions. Writing was done by KOD, HE, AH, MFS, and BF. Data were curated by KOD, HE, and BF. Original draft preparation and software development were done by KOD. Method development was done by KOD, HE, and AH. Investigation and formal analysis were done by KOD, HE, AH, MFS, and BF. Visualization was done by KOD. The project was administrated and supervised by KOD, HE, AH, MD, and BF. Resources and funding were acquired by MD and BF. KOD, HE, AH, MFS, MD, AR, and BF contributed to reviewing and editing the manuscript.

Competing interests. The corresponding author declares that none of the authors has any competing interests.

Acknowledgements. We want to thank the late Pär Jansson for initial discussions on combining M2PG1 with OpenDrift. KOD wants to thank Martin Arntsen for having the initial idea of using OpenDrift for this project and helping to sketch out the overarching themes of the framework. We want to thank Jon Albretsen and the Institute of Marine Research for sharing NorKyst simulations. Claude 3.5 Sonnet assisted the process of writing the code associated with this manuscript and GPT 4.0 to proofread and reformulate certain sentences and/or paragraphs in the text. This study is funded by the Research Council of Norway through EMAN7 (Environmental impact of Methane seepage and sub-seabed characterization at LoVe-Node 7, project number 320100) and ReGAME (Reliable global methane emissions estimates in a changing world, project number 325610).

https://doi.org/10.5194/egusphere-2025-998
Preprint. Discussion started: 26 March 2025
© Author(s) 2025. CC BY 4.0 License.

References

Aghito, M., Calgaro, L., Dagestad, K.-F., Ferrarin, C., Marcomini, A., Breivik, Ø., and Hole, L. R.: ChemicalDrift 1.0: an open-source Lagrangian chemical-fate and transport model for organic aquatic pollutants, Geoscientific Model Development, 16, 2477–2494, https://doi.org/10.5194/gmd-16-2477-2023, 2023.

Albretsen, J., Sperrevik, A. K., Staalstrøm, A., Sandvik, A. D., Vikebø, F., and Asplin, L.: NordKyst-800 Report No. 1 User Manual and technical descriptions, Tech. Rep. 2, 2011.

Bresenham, J. E.: Algorithm for computer control of a digital plotter, IBM Systems Journal, 4, 25–30, https://doi.org/10.1147/sj.41.0025, 1965.

Chan, E. W., Shiller, A. M., Joung, D. J., Arrington, E. C., Valentine, D. L., Redmond, M. C., Breier, J. A., Socolofsky, S. A., and Kessler, J. D.: Investigations of Aerobic Methane Oxidation in Two Marine Seep Environments: Part 2—Isotopic Kinetics, Journal of Geophysical Research: Oceans, 124, 8392–8399, https://doi.org/https://doi.org/10.1029/2019JC015603, 2019.

Chand, S., Rise, L., Bellec, V., Dolan, M., Bøe, R., Thorsnes, T., Buhl-Mortensen, P., and Buhl-Mortensen, L.: Active venting system offshore northern Norway, Eos, 89, 261–262, https://doi.org/10.1029/2008EO290001, 2008.

Dagestad, K. F., Röhrs, J., Breivik, O., and Ådlandsvik, B.: OpenDrift v1.0: A generic framework for trajectory modelling, Geoscientific Model Development, 11, 1405–1420, https://doi.org/10.5194/gmd-11-1405-2018, 2018.

de Angelis, M. A., Lilley, M. D., and Baross, J. A.: Methane oxidation in deep-sea hydrothermal plumes of the endeavour segment of the Juan de Fuca Ridge, Deep Sea Research Part I: Oceanographic Research Papers, 40, 1169–1186, https://doi.org/10.1016/0967-0637(93)90132-M, 1993.

de Groot, T. R., Kalenitchenko, D., Moser, M., Argentino, C., Panieri, G., Lindgren, M., Dølven, K. O., Ferré, B., Svenning, M. M., and Niemann, H.: Methanotroph activity and connectivity between two seep systems north off Svalbard, Frontiers in Earth Science, 12, https://doi.org/10.3389/feart.2024.1287226, publisher: Frontiers, 2024.

De Haan, P.: On the use of density kernels for concentration estimations within particle and puff dispersion models, Atmospheric Environment, 33, 2007–2021, https://doi.org/10.1016/S1352-2310(98)00424-5, 1999.

Dugstad, J. S., Isachsen, P. E., and Fer, I.: The mesoscale eddy field in the Lofoten Basin from high-resolution Lagrangian simulations, Ocean Science, 17, 651–674, https://doi.org/10.5194/os-17-651-2021, 2021.

Fan, L. and Tsuchiya, K.: Bubble wake dynamics in Liquids and Liquid Solid Suspensions, Butterworth-Heinemann, Stoneham, MA, USA, 1990.

Ferre, B., Jansson, P., Moser, M., Portnov, A., Graves, C., Panieri, G., Gründger, F., Berndt, C., Lehmann, M., and Niemann, H.: Reduced methane seepage from Arctic sediments during cold bottom-water conditions, Nature Geoscience, 13, https://doi.org/10.1038/s41561-019-0515-3, 2020.

Ferré, B., Barreyre, T., Bünz, S., Argentino, C., Corrales-Guerrero, J., Dølven, K. O., Stetzler, M., Fallati, L., Sert, M. F., Panieri, G., Rastrick, S., Kutti, T., and Moser, M.: Contrasting Methane Seepage Dynamics in the Hola Trough Offshore Norway: Insights From Two Different Summers, Journal of Geophysical Research: Oceans, 129, e2024JC020 949, https://doi.org/https://doi.org/10.1029/2024JC020949, e2024JC020949 2024JC020949, 2024.

Frisch, U.: Turbulence, Cambridge University Press, New York, NY, USA, 1995.

https://doi.org/10.5194/egusphere-2025-998
Preprint. Discussion started: 26 March 2025
© Author(s) 2025. CC BY 4.0 License.

Gentz, T., Damm, E., Schneider von Deimling, J., Mau, S., McGinnis, D. F., and Schlüter, M.: A water column study of methane around gas flares located at the West Spitsbergen continental margin, Continental Shelf Research, 72, 107–118, https://doi.org/10.1016/j.csr.2013.07.013, 2014.

Graves, C. A., Lea, S., Gregor, R., Helge, N., P., C. D., David, L., E., F. R., W., S. A., Heiko, S., and H., J. R.: Fluxes and fate of dissolved methane released at the seafloor at the landward limit of the gas hydrate stability zone offshore western Svalbard, Journal of Geophysical Research: Oceans, 120, 6185–6201, https://doi.org/10.1002/2015JC011084, 2015.

Griffiths, R. P., Caldwell, B. A., Cline, J. D., Broich, W. A., and Morita, R. Y.: Field Observations of Methane Concentrations and Oxidation Rates in the Southeastern Bering Sea, Applied and Environmental Microbiology, 44, 435–446, 1982.

Gründger, F., Probandt, D., Knittel, K., Carrier, V., Kalenitchenko, D., Silyakova, A., Serov, P., Ferré, B., Svenning, M. M., and Niemann, H.: Seasonal shifts of microbial methane oxidation in Arctic shelf waters above gas seeps, Limnology and Oceanography, n/a, https://doi.org/https://doi.org/10.1002/lno.11731, 2021.

Hersbach, H., Bell, B., Berrisford, P., Biavati, G., Horányi, A., Muñoz Sabater, J., Nicolas, J., Peubey, C., Radu, R., Rozum, I., Schepers, D., Simmons, A., Soci, C., Dee, D., and Thépaut, J.-N.: ERA5 hourly data on single levels from 1940 to present, https://doi.org/10.24381/cds.adbb2d47, 2023.

Jakobsson, M., Mayer, L. A., Coakley, B., Dowdeswell, J. A., Forbes, S., Fridman, B., Hodnesdal, H., Noormets, R., Pedersen, R., Rebesco, M., Schenke, H.-W., Zarayskaya A, Y., Accettella, D., Armstrong, A., Anderson, R. M., Bienhoff, P., Camerlenghi, A., Church, I., Edwards, M., Gardner, J. V., Hall, J. K., Hell, B., Hestvik, O. B., Kristoffersen, Y., Marcussen, C., Mohammad, R., Mosher, D., Nghiem, S. V., Pedrosa, M. T., Travaglini, P. G., and Weatherall, P.: The International Bathymetric Chart of the Arctic Ocean (IBCAO) Version 3.0, Geophysical Research Letters, https://doi.org/10.1029/2012GL052219, 2012.

James, R. H., Bousquet, P., Bussmann, I., Haeckel, M., Kipfer, R., Leifer, I., Niemann, H., Ostrovsky, I., Piskozub, J., Rehder, G., Treude, T., Vielstädte, L., and Greinert, J.: Effects of climate change on methane emissions from seafloor sediments in the Arctic Ocean: A review, Limnology and Oceanography, 61, S283–S299, https://doi.org/https://doi.org/10.1002/lno.10307, 2016.

Jansson, P., Ferré, B., Silyakova, A., Dølven, K., and Omstedt, A.: A new numerical model for understanding free and dissolved gas progression toward the atmosphere in aquatic methane seepage systems, Limnology and Oceanography: Methods, 17, https://doi.org/10.1002/lom3.10307, 2019.

Kish, L.: Survey Sampling, John Wiley and Sons Inc., New York, ISBN 047148900X, 1965.

Larsen, Y., Hanssen, A., Krane, B., Pécseli, H. L., and Trulsen, J.: Time-resolved statistical analysis of nonlinear electrostatic fluctuations in the ionospheric E region, Journal of Geophysical Research: Space Physics, 107, https://doi.org/10.1029/2001JA900125, 2002.

Leblond, I., Scalabrin, C., and Berger, L.: Acoustic monitoring of gas emissions from the seafloor. Part I: Quantifying the volumetric flow of bubbles, Marine Geophysical Research, 35, 191–210, https://doi.org/10.1007/s11001-014-9223-y, 2014.

Leifer, I. and Patro, R. K.: The bubble mechanism for methane transport from the shallow sea bed to the surface: A review and sensitivity study, Continental Shelf Research, 22, 2409–2428, https://doi.org/https://doi.org/10.1016/S0278-4343(02)00065-1, 2002.

Mau, S., Heintz, M. B., and Valentine, D. L.: Quantification of CH4 loss and transport in dissolved plumes of the Santa Barbara Channel, California, Continental Shelf Research, 32, 110–120, https://doi.org/10.1016/j.csr.2011.10.016, 2012.

Mau, S., Blees, J., Helmke, E., Niemann, H., and Damm, E.: Vertical distribution of methane oxidation and methanotrophic response to elevated methane concentrations in stratified waters of the Arctic fjord Storfjorden (Svalbard, Norway), Biogeosciences, 10, 6267–6278, https://doi.org/10.5194/bg-10-6267-2013, 2013.

https://doi.org/10.5194/egusphere-2025-998
Preprint. Discussion started: 26 March 2025
© Author(s) 2025. CC BY 4.0 License.

Mau, S., Römer, M., Torres, M. E., Bussmann, I., Pape, T., Damm, E., Geprägs, P., Wintersteller, P., Hsu, C.-W., Loher, M., and Bohrmann, G.: Widespread methane seepage along the continental margin off Svalbard - from Bjørnøya to Kongsfjorden, Scientific Reports, 7, 42 997, https://doi.org/10.1038/srep42997, 2017.

Mau, S., Tu, T.-H., Becker, M., dos Santos Ferreira, C., Chen, J.-N., Lin, L.-H., Wang, P.-L., Lin, S., and Bohrmann, G.: Methane Seeps and Independent Methane Plumes in the South China Sea Offshore Taiwan, Frontiers in Marine Science, 7, https://doi.org/10.3389/fmars.2020.00543, publisher: Frontiers, 2020.

McGinnis, D. F., Greinert, J., Artemov, Y., Beaubien, S. E., and Wüest, A.: Fate of rising methane bubbles in stratified waters: How much methane reaches the atmosphere?, Journal of Geophysical Research: Oceans, 111, https://doi.org/10.1029/2005JC003183, 2006.

Myhre, C. L., Ferré, B., Platt, S. M., Silyakova, A., Hermansen, O., Allen, G., Pisso, I., Schmidbauer, N., Stohl, A., Pitt, J., Jansson, P., Greinert, J., Percival, C., Fjaeraa, A. M., O'Shea, S. J., Gallagher, M., Le Breton, M., Bower, K. N., Bauguitte, S. J. B., Dalsøren, S., Vadakkepuliyambatta, S., Fisher, R. E., Nisbet, E. G., Lowry, D., Myhre, G., Pyle, J. A., Cain, M., and Mienert, J.: Extensive release of methane from Arctic seabed west of Svalbard during summer 2014 does not influence the atmosphere, Geophysical Research Letters, 43, 4624–4631, https://doi.org/https://doi.org/10.1002/2016GL068999, 2016.

Pack, M. A., Heintz, M. B., Reeburgh, W. S., Trumbore, S. E., Valentine, D. L., Xu, X., and Druffel, E. R. M.: Methane oxidation in the eastern tropical North Pacific Ocean water column, Journal of Geophysical Research: Biogeosciences, 120, 1078–1092, https://doi.org/10.1002/2014JG002900, _eprint: https://onlinelibrary.wiley.com/doi/pdf/10.1002/2014JG002900, 2015.

Percival, D. B. and Walden, A. T.: Spectral Analysis for Physical Applications, Cambridge University Press, Cambridge, UK, 1993.

Pécseli, H.: Fluctuations in Physical Systems, Cambridge University Press, Cambridge, UK, 2000.

Ruppel, C. D. and Kessler, J. D.: The interaction of climate change and methane hydrates, Reviews of Geophysics, 55, 126–168, https://doi.org/https://doi.org/10.1002/2016RG000534, 2017.

Sansone, F. J. and Martens, C. S.: Methane oxidation in Cape Lookout Bight, North Carolina, Limnology and Oceanography, 23, 349–355, https://doi.org/10.4319/lo.1978.23.2.0349, _eprint: https://onlinelibrary.wiley.com/doi/pdf/10.4319/lo.1978.23.2.0349, 1978.

SciPy Community: SciPy: Scientific Library for Python - `scipy.stats.gaussian_kde` function, https://docs.scipy.org/doc/scipy/reference/generated/scipy.stats.gaussian_kde.html, accessed: 2024-09-20, 2024.

Serov, P., Portnov, A., Mienert, J., Semenov, P., and Ilatovskaya, P.: Methane release from pingo-like features across the South Kara Sea shelf, an area of thawing offshore permafrost, Journal of Geophysical Research: Earth Surface, 120, 1515–1529, https://doi.org/https://doi.org/10.1002/2015JF003467, 2015.

Sert, M. F., D'Andrilli, J., Gründger, F., Niemann, H., Granskog, M. A., Pavlov, A. K., Ferré, B., and Silyakova, A.: Compositional Differences in Dissolved Organic Matter Between Arctic Cold Seeps Versus Non-Seep Sites at the Svalbard Continental Margin and the Barents Sea, Frontiers in Earth Science, 8, 552 731, https://doi.org/10.3389/feart.2020.552731, publisher: Frontiers, 2020.

Sert, M. F., Schweitzer, H. D., de Groot, T. R., Kekäläinen, T., Jänis, J., Bernstein, H. C., Ferré, B., Gründger, F., Kalenitchenko, D., and Niemann, H.: Elevated methane alters dissolved organic matter composition in the Arctic Ocean cold seeps, Frontiers in Earth Science, 11, https://www.frontiersin.org/articles/10.3389/feart.2023.1290882, 2023.

Shchepetkin, A. F. and McWilliams, J. C.: The regional oceanic modeling system (ROMS): a split-explicit, free-surface, topography-following-coordinate oceanic model, Ocean Modelling, 9, 347–404, https://doi.org/https://doi.org/10.1016/j.ocemod.2004.08.002, 2005.

Silverman, B. W.: Density Estimation for Statistics and Data Analysis, Chapman & Hall, London, 1986.

https://doi.org/10.5194/egusphere-2025-998
Preprint. Discussion started: 26 March 2025
© Author(s) 2025. CC BY 4.0 License.

Silyakova, A., Jansson, P., Serov, P., Ferré, B., Pavlov, A. K., Hattermann, T., Graves, C. A., Platt, S. M., Myhre, C. L., Gründger, F., and Niemann, H.: Physical controls of dynamics of methane venting from a shallow seep area west of Svalbard, Continental Shelf Research, 194, 104 030, https://doi.org/10.1016/j.csr.2019.104030, 2020.

Slagstad, D., Tande, K. S., and Wassman, P.: Modelled carbon fluxes as validated by field dta on the north Norwegian shelf during the productive period in 1994, Sarsia, 84, 303–317, https://doi.org/10.1080/00364827.1999.10420434, 1999.

Sole-Mari, G., Bolster, D., Fernàndez-Garcia, D., and Sanchez-Vila, X.: Particle density estimation with grid-projected and boundary-corrected adaptive kernels, Advances in Water Resources, 131, 103 382, https://doi.org/10.1016/j.advwatres.2019.103382, 2019.

Steinle, L., Schmidt, M., Bryant, L., Haeckel, M., Linke, P., Sommer, S., Zopfi, J., Lehmann, M. F., Treude, T., and Niemannn, H.: Linked sediment and water-column methanotrophy at a man-made gas blowout in the North Sea: Implications for methane budgeting in seasonally stratified shallow seas: Linked sediment and water methanotrophy, Limnology and Oceanography, 61, S367–S386, https://doi.org/10.1002/lno.10388, 2016.

Steinle, L., Maltby, J., Treude, T., Kock, A., Bange, H. W., Engbersen, N., Zopfi, J., Lehmann, M. F., and Niemann, H.: Effects of low oxygen concentrations on aerobic methane oxidation in seasonally hypoxic coastal waters, Biogeosciences, 14, 1631–1645, https://doi.org/https://doi.org/10.5194/bg-14-1631-2017, 2017.

Thompson, R. and Stohl, A.: FLEXINVERT: An atmospheric Bayesian inversion framework for determining surface fluxes of trace species using an optimized grid, Geoscientific Model Development Discussions, 7, 3751–3801, https://doi.org/10.5194/gmdd-7-3751-2014, 2014.

Torsæter, M., Bello-Palacios, A., Borgerud, L., Nygård, O.-K., Frost, T., Hofstad, H., and Andrews, J.: Evaluating legacy well leakage risk in CO_2 storage, Proc. 17th Int. Conf. on Greenhouse Gas Control Technologies, p. 19pp, https://doi.org/10.2139/ssrn.5062896, 2024.

Uhlig, C., Kirkpatrick, J. B., D'Hondt, S., and Loose, B.: Methane-oxidizing seawater microbial communities from an Arctic shelf, Biogeosciences, 15, 3311–3329, https://doi.org/10.5194/bg-15-3311-2018, publisher: Copernicus GmbH, 2018.

Umlauf, L. and Burchard, H.: A generic length-scale equation for geophysical turbulence models, Journal of Marine Research, 61, 235–265, https://doi.org/10.1357/002224003322005087, 2003.

Valentine, D. L., Kessler, J. D., Redmond, M. C., Mendes, S. D., Heintz, M. B., Farwell, C., Hu, L., Kinnaman, F. S., Yvon-Lewis, S., Du, M., Chan, E. W., Tigreros, F. G., and Villanueva, C. J.: Propane Respiration Jump-Starts Microbial Response to a Deep Oil Spill, Science, 330, 208–211, https://doi.org/10.1126/science.1196830, publisher: American Association for the Advancement of Science, 2010.

Vardeman, S.: Sheppard's correction for variances and the "quantization noise model", IEEE Transactions on Instrumentation and Measurement, 54, 2117–2119, https://doi.org/10.1109/TIM.2005.853348, 2005.

Veloso, M., Greinert, J., Mienert, J., and Batist, M.: A new methodology for quantifying bubble flow rates in deep water using splitbeam echosounders: Examples from the Arctic offshore NW-Svalbard, Limnology and Oceanography: Methods, 13, 2015.

Wanninkhof, R.: Relationship between wind speed and gas exchange over the ocean revisited, Limnology and Oceanography: Methods, 12, 351–362, https://doi.org/10.4319/lom.2014.12.351, 2014.

Ward, B. B., Kilpatrick, K. A., Novelli, P. C., and Scranton, M. I.: Methane oxidation and methane fluxes in the ocean surface layer and deep anoxic waters, Nature, 327, 226–229, https://doi.org/10.1038/327226a0, publisher: Nature Publishing Group, 1987.

Ward, B. B., Kilpatrick, K. A., Wopat, A. E., Minnich, E. C., and Lidstrom, M. E.: Methane oxidation in Saanich inlet during summer stratification, Continental Shelf Research, 9, 65–75, https://doi.org/10.1016/0278-4343(89)90083-6, 1989.

Weinstein, A., Navarrete, L., Ruppel, C., Weber, T. C., Leonte, M., Kellermann, M. Y., Arrington, E. C., Valentine, D. L., Scranton, M. I., and Kessler, J. D.: Determining the flux of methane into Hudson Canyon at the edge of methane

https://doi.org/10.5194/egusphere-2025-998
Preprint. Discussion started: 26 March 2025
© Author(s) 2025. CC BY 4.0 License.

clathrate hydrate stability, Geochemistry, Geophysics, Geosystems, 17, 3882–3892, https://doi.org/10.1002/2016GC006421, _eprint: https://onlinelibrary.wiley.com/doi/pdf/10.1002/2016GC006421, 2016.

Yaglom, A.: Correlation Theory of Stationary and Related Random Functions, Springer-Verlag, New York, NY, 1987.

https://doi.org/10.5194/egusphere-2025-998
Preprint. Discussion started: 26 March 2025
© Author(s) 2025. CC BY 4.0 License.

Location	Temp (°C)	ϕ (nM)	k_{ox} $10^{-6}s^{-1}$	$t_{0.5}$ (days)	Reference
Oxic/anoxic interface					
Cariaco Trench, Caribbean Sea	-	<12100	0.03	277	Ward et al. (1987)
Saanich Inlet, British Columbia	9	<1580	0.02	535	Ward et al. (1989)
Eastern Tropical North Pacific	-	19	0.10	77	Pack et al. (2015)
Hydrothermal plume					
Juan De Fuca v.	-	<390	1.74	5	de Angelis et al. (1993)
Man-made accidents					
Deepwater Horizon, Gulf of Mexico	-	<183000	0.73	11	Valentine et al. (2010)
North Sea gas blowout	10	<42097	0.41	20	Steinle et al. (2016)
Seep environment					
Cape Lookout Bight, North Carolina	23-27	<740	0.08	107	Sansone & Martens (1978)
Santa Barbara Channel, California	5-16	<1900	0.09	93	Mau et al. (2012)
Boknis Eck, Baltic Sea	1-3	300-466	0.50	16	Steinle et al. (2017)
South China Sea	2-5	<1000	0.04	229	Mau et al. (2020)
Hudson Canyon, US Atlantic	-	<335	0.93	9	Weinstein et al. (2016)
Elson Lagoon, Alaska	-1.8	<53.8	0.12	69	Uhlig et al. (2018)
Cold seeps - Svalbard Continental margin					
Norskebanken	4.7	<83.1	0.06	125	Sert et al. (2023)
Hinlopen Trough	3.5	<874	0.23	35	De Groot et al. (2024)
Prins Karl Forland (2015)	∼3	<334	0.98	8	Gründger et al., (2021)
Prins Karl Forland (2016)	∼1.5	<437	0.02	433	Gründger et al., (2021)
Prins Karl Forland (2017)	∼3	<262	0.02	385	Gründger et al., (2021)
Prins Karl Forland	1.6-4.8	<524	0.21	38	Gentz et al. (2014)
Hornsundbanken	>3	<878	0.41	20	Mau et al. (2017)
Isfjordenbanken	>3	<100	0.62	13	Mau et al. (2017)
Storfjordrenna	-0.5	<82	0.22	36	Sert et al. (2020)
Storfjorden	-1.5	<72.3	0.35	23	Mau et al. (2013)

Table E1. Methane Oxidation Rate Coefficients (k_{ox}) in units of 10^{-6} s^{-1} (μHz) from various studies. We have obtained the maximum k_{ox} reported in the studies unless ranges are given. Half-lives are calculated by solving for $\phi(t_{0.5}) = 0.5\phi_0$ in Eq. (E1), i.e. $t_{0.5} = \ln(2)/k_{ox}$. In Gründker et al., 2021 only May data was included from 2016 and the difference in turnover time between 2016 and 2017 is because the maximum rate coefficient was 1.85×10^{-8} s^{-1} in 2016 and 2.01×10^{-8} s^{-1} in 2017, but this difference is rounded off in the table.